nature communications

Article

https://doi.org/10.1038/s41467-025-57499-x

Janus hydrogel microrobots with bioactive ions for the regeneration of tendon-bone interface

Received: 25 April 2024

Accepted: 25 February 2025

Published online: 04 March 2025

Check for updates

Zichuan Ding[1,2,7], Yongrui Cai[1,7], Haocheng Sun[1], Xiao Rong[2], Sipei Ye[3], Jiaxuan Fan[1], Yahao Lai[1], Zhimin Liang[4], Chao Huang[1], Peilin Li[5], Xiaoxue Fu[1], Liu Wang[3], Guosheng Tang[6] ✉, Zongke Zhou[1] ✉ & Zeyu Luo[1] ✉

Regenerating natural gradients of the tendon–bone interface (TBI) is a major challenge in the reconstruction of rotator cuff tear (RCT). In this study, magnetic Janus hydrogel microrobots to match the TBI orientation during RCT reconstruction surgery are developed via a biofriendly gas-shearing microfluidic platform. Through separate loading of Mg^{2+} and Zn^{2+}, the microrobots facilitate the immediate restoration and long-term maintenance of the natural mineral gradient in the TBI after implantation and alignment through magnetic manipulation. In vitro studies confirm the spatiotemporal cell phenotype modulation effects of the microrobots. In a rat RCT model, microrobots synchronously promote the bone and tendon regeneration, and the restoration of gradient tendon–bone transition structures in the TBI. Overall, by rebuilding the Mg^{2+}/Zn^{2+} mineral gradient, cell phenotype gradient and structural gradient of the TBI, magnetic Janus microrobots loaded with dual bioactive ions represent a promising strategy for promoting TBI healing in RCT reconstruction surgery.

Rotator cuff tear (RCT) is the predominant cause of shoulder joint disability and are particularly prevalent among the elderly population. The incidence of full-thickness RCT among the general population exceeds 20%, with a notable increase in those aged 80 years and above, where the proportion even surpasses 50%[1]. Given the limited inherent capacity for intrinsic healing of the rotator cuff, reconstruction surgery is often required after RCT to restore the structural integrity of the rotator cuff and achieve better clinical outcomes for affected patients[2]. Nevertheless, despite concerted endeavors directed toward refining surgical techniques and postoperative rehabilitation, the reported failure rates of RCT reconstruction are still as high as 20%-70%[3], primarily due to the poor healing of the tendon–bone interface (TBI) after surgical intervention[4]. The TBI is a hierarchical transition tissue spanning the submillimeter dimension characterized by natural gradients in composition, cell phenotype, and structure from the tendon to the bone[5,6]. The variations in the composition of the TBI, especially the contents of minerals such as Ca^{2+}, Mg^{2+}, and Zn^{2+}, constitute the natural composition gradient of the TBI[7–9]. In addition, bone tissue is characterized primarily by a high presence of terminally differentiated cells derived from bone mesenchymal stem cells (BMSCs), and tendon

[1]Orthopaedic Research Institute, Department of Orthopaedics, West China Hospital, Sichuan University, Chengdu, China. [2]Department of Medical Ultrasound, West China Hospital, Sichuan University, Chengdu, China. [3]CAS Key Laboratory of Mechanical Behavior and Design of Materials, Department of Modern Mechanics, University of Science and Technology of China, Hefei, China. [4]West China School of Nursing, Sichuan University, Chengdu, China. [5]State Key Laboratory of Oral Diseases & National Center for Stomatology & National Clinical Research Center for Oral Diseases & West China Hospital of Stomatology, Sichuan University, Chengdu, China. [6]Guangzhou Municipal and Guangdong Provincial Key Laboratory of Molecular Target & Clinical Pharmacology, the NMPA and State Key Laboratory of Respiratory Disease, the Fifth Affiliated Hospital and School of Pharmaceutical Sciences, Guangzhou Medical University, Guangzhou, China. [7]These authors contributed equally: Zichuan Ding, Yongrui Cai. ✉e-mail: guoshengtang@gzhmu.edu.cn; zhouzongke@scu.edu.cn; luozy@wchscu.edu.cn

tissue is rich in active tenocytes (TCs), representing the main manifestation of the cell phenotype gradient in the TBI[6,9]. Furthermore, the gradual changes in the orientation of collagen fibers from tendon with highly aligned collagen fibers to bone with less organized collagen fibers are the primary reasons for the formation of the structural gradient[5,10]. The gradient in mineral content plays a key role in the formation and maintenance of the cell phenotype gradient, which in turn is responsible for the formation and reconstruction of the tendon–bone transition structure in the TBI[5,6,11,12]. To date, the key challenge of RCT reconstruction still lies in developing effective strategies to rebuild these gradients in the TBI and thus achieve better TBI healing effects.

Bioactive metal ions have garnered considerable attention for their role in facilitating tissue regeneration. Variations in the content of various bioactive metal ions across different tissues exist, each exhibiting specialized functions in maintaining the normal physiological function of tissues and fostering tissue regenerative processes. Researchers have reported a significantly greater Mg^{2+}/Zn^{2+} ratio in human bone tissue than in tendon tissue, indicating a natural gradient in their content in the TBI[13,14]. Magnesium, an essential element for the human body, primarily resides in the skeletal system and plays a pivotal role in bone development, metabolism, and regeneration[15]. Mg^{2+} can accelerate bone regeneration by promoting the proliferation, accumulation, and osteogenic differentiation of BMSCs[16]; suppressing osteoclast activity[17]; and regulating the metabolism and functionality of parathyroid hormone and vitamin D[18]. Zinc, which is abundant in tendons and muscles, serves as a cofactor for numerous transcription factors and enzyme systems that participate in collagen metabolism and tissue regeneration[19]. Zn^{2+} can stimulate TCs proliferation, accumulation, and tenogenesis-related functions, which substantially increase the content of type-I collagen (COL-I) within injured tendon tissues while restraining the synthesis and accumulation of type-III collagen (COL-III), consequently expediting the tendon repair process[20,21]. Although Mg^{2+} and Zn^{2+} have been proven to promote bone and tendon regeneration, respectively, effectively combining these ions to achieve satisfactory TBI repair remains a major challenge because of the abovementioned natural Mg^{2+}/Zn^{2+} gradient in TBI. The fabrication of Janus-structured materials with a Mg^{2+}/Zn^{2+} gradient offers a strategy for promoting RCT reconstruction[22–24].

Although previous studies have reported the fabrication of double- or triple-layered hydrogels with ion[21], growth factor[25], cell[26], or matrix[27] gradients by molding or 3D (bio)printing methods to rebuild the gradients of TBI, the application of these hydrogels in RCT reconstruction remains unsatisfactory. This issue is primarily due to the widespread adoption of minimally invasive surgery and the use of endoscopes in RCT reconstruction surgery, making the implantation of these complex structured hydrogels without injectability difficult. Additionally, adjusting the orientation of these hydrogels to match the gradients of the TBI during and after surgery is very difficult. Currently, the development of more effective and applicable biomaterials that can rebuild the natural mineral composition gradient of TBI in RCT reconstruction surgery is urgently needed but highly challenging. Microrobots are materials at the micron scale capable of movement within the body, with magnetic control being one of the most widely employed methods for manipulation[28,29]. By exploiting therapeutic cargo loading and noncontact manipulation properties[30,31], microrobots can serve as precise, practical, and convenient surgical tools in RCT reconstruction surgery.

In this work, we fabricate magnetic Janus hydrogel microrobots by loading with $Mg_3(PO_4)_2$ (MgP) & Fe_3O_4 nanoparticles (Fe-NPs) or ZnO nanoparticles (Zn-NPs) in two independent compartments of the hydrogel microspheres. The biofriendly multicompartmental alginate-based microspheres is produced through an oil-free gas-shearing microfluidic platform. After the microrobots are implanted to the TBI in RCT reconstruction surgery, they are controlled to align with the TBI orientation with an external magnetic field (bone side with Mg^{2+} of microrobots toward the bone defect area and tendon side with Zn^{2+} toward the tendon injury area). The microrobots facilitate the immediate restoration of the natural Mg^{2+}/Zn^{2+} gradient in the TBI after implantation, and the effect can be maintained over 14 days. The microrobots further show spatiotemporal cell phenotype modulation effects in vitro: hemispheres loaded with Mg^{2+} and Zn^{2+} promote the proliferation, migration and function of BMSCs and TCs, respectively, thus reconstructing the cell phenotype gradient and orchestrating the synchronous regeneration of tendon and bone. The significant effect of microrobots on the restoration of the gradient tendon–bone transition structure of the TBI and the promotion of TBI healing is further proven in a rat RCT model (Fig. 1). Magnetic Janus microrobots loaded with dual bioactive ions provide a promising strategy for promoting TBI healing in RCT reconstruction surgery and present a promising paradigm for clinical translation and applications.

Results and Discussion

Characterization of the loaded nanoparticles

Scanning electron microscopy (SEM) and transmission electron microscopy (TEM) images revealed that the Zn-NPs possessed a cylindrical morphology with a size of several hundred nanometers (Supplementary Fig. 1A, B). Energy dispersive spectroscopy (EDS) revealed a uniform distribution of Zn and O in the Zn-NPs (Supplementary Fig. 1A-B). The range of their hydrated particle sizes was from 200 nm to 700 nm according to dynamic light scattering (DLS) measurements (Supplementary Fig. 1C). X-ray diffraction (XRD) revealed that the patterns of the Zn-NPs conformed to the standard pattern of ZnO nanoparticles (Supplementary Fig. 1D)[32,33]. The morphology of the Fe-NPs was also characterized via SEM and TEM, and the results revealed that the Fe-NPs were spherical-shaped nanoparticles several tens of nanometers in size (Supplementary Fig. 2A, B). EDS revealed a uniform distribution of Fe and O (Supplementary Fig. 2A, B). DLS demonstrated that the hydrated sizes of the Fe-NPs ranged from 40 nm to 90 nm (Supplementary Fig. 2C). XRD revealed that the sites and intensities of the diffraction peaks of the Fe-NPs are consistent with the standard pattern for Fe_3O_4 nanoparticles (Supplementary Fig. 2D)[34–36]. The sharp peaks indicate the high crystallinity of the Fe-NPs. The magnetic properties of the Fe-NPs were measured via vibrating sample magnetometer (VSM) at room temperature (Supplementary Fig. 2E, F). The amounts of coercive force (Hc), saturation magnetization (Ms), and remanent magnetization (Mr) were 141.51 Oe, 75.57 emu/g, and 15.37 emu/g, respectively, indicating that the Fe-NPs exhibited sufficient magnetization power and could be simply attracted by a magnet. Therefore, Fe-NPs are suitable for loading into microrobots for magnetic manipulation[35,36].

Fabrication of Janus hydrogel microrobots

Figures 1A and 2A show the scheme of the gas-shearing microfluidic platform and the fabrication process of magnetic Janus microrobots loaded with two bioactive ions. Briefly, two syringes loaded with different pre-gel solutions (alginate with MgP & Fe-NPs or Zn-NPs) and controlled with a digital injection pump were connected to two independent needles. The liquid-flow needles were inserted coaxially into a shell, and the nitrogen gas was transported through the space between the needles and shell, generating a shearing force to induce the formation of alginate droplets. $CaCl_2$ was used in a collection bath to crosslink the alginate droplets. The equipment and microrobots produced in the Petri dish are shown in Supplementary Fig. 3. Microrobots with high monodispersity presented a regular Janus structure under confocal laser scanning microscopy (CLSM), light microscopy and fluorescence microscopy (Fig. 2B–D and Supplementary Fig. 4). The size of the microrobots can be easily controlled by adjusting the nitrogen gas flow (gas flow: 7 L/min, microrobot size: 381.3 ± 21.5 μm; gas flow: 5 L/min, microrobot size: 450.4 ± 13.7 μm; gas flow: 3 L/min, microrobot size:

https://doi.org/10.1038/s41467-025-57499-x

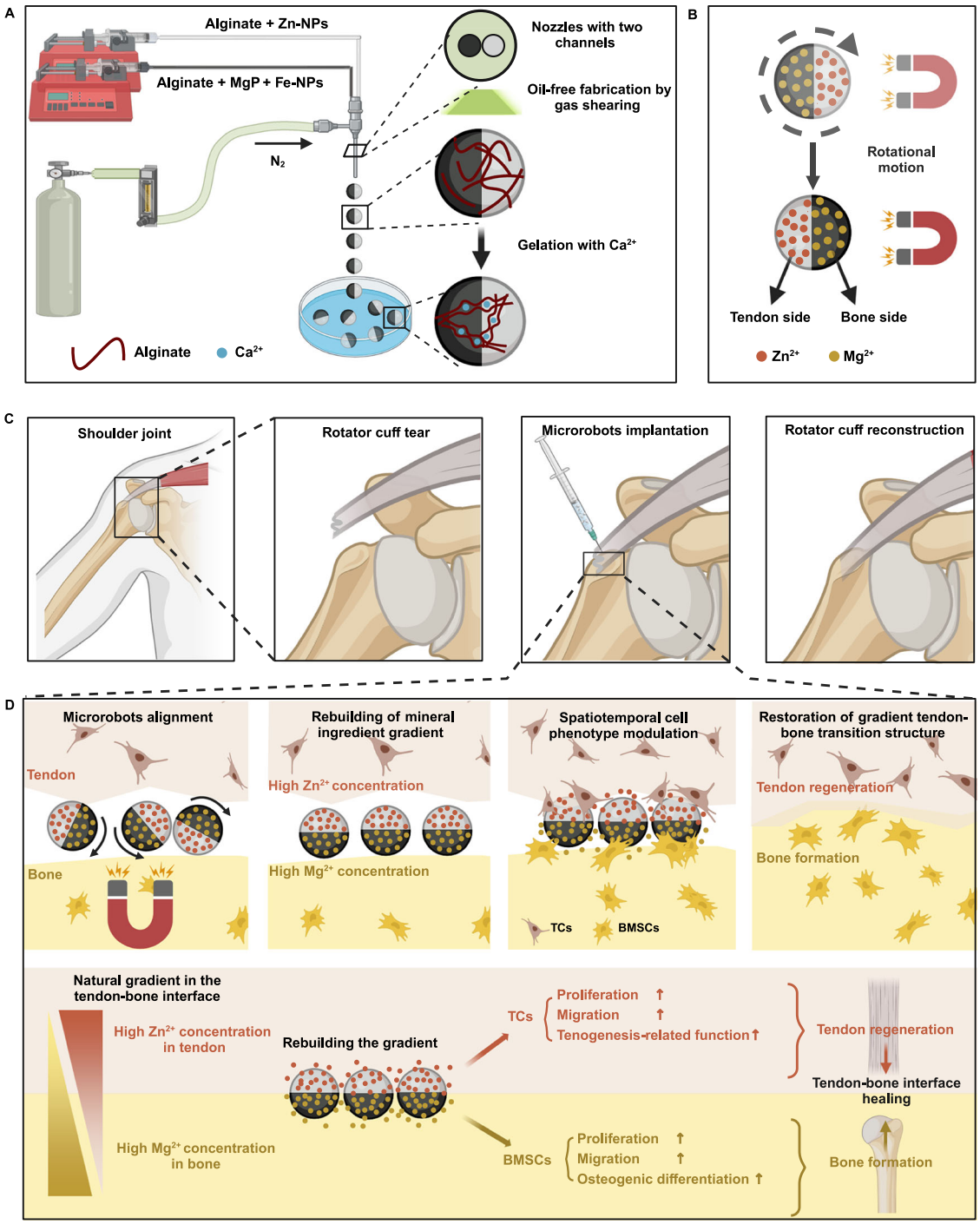

Fig. 1 | Magnetic Janus hydrogel microrobots for the regeneration of gradients in the TBI. A Equipment and fabrication of magnetic Janus hydrogel microrobots by gas shearing. **B** Motion behavior of the microrobots under an external magnetic field. **C** Application of the microrobots in RCT reconstruction surgery. **D** Therapeutic effect and underlying mechanism of the microrobots in the regeneration of gradients in the TBI. Through rebuilding of the Mg^{2+}/Zn^{2+} mineral gradient, spatiotemporally modulating the cell phenotypes of BMSCs and TCs, synchronously regenerating bone and tendon, and restoring the gradient tendon–bone transition structure of the TBI, microrobots eventually promote TBI healing. MgP: $Mg_3(PO_4)_2$, Fe-NPs: Fe_3O_4 nanoparticles, Zn-NPs: ZnO nanoparticles, BMSCs: bone mesenchymal stem cells, TCs: tenocytes. Created in BioRender. Ding, Z. (2025) https://BioRender.com/p43d624.

725.0 ± 36.0 μm) (Fig. 2B–D). As the alginate droplet grows on the needle tip, its diameter increases, and the shearing force of nitrogen gas flow on it also increases[37]. When the gas-shearing force overcomes the resistance force by surface tension of the droplet, the droplet is detached from the needle tip and falls into the collection bath[37]. As a result, increasing the nitrogen gas flow allows droplets to detach from the needle at a smaller diameter, thereby producing microrobots with smaller diameters. Microrobots of different sizes maintain consistent and excellent injectability (Supplementary Movie 1). The fabrication of such a broad range of injectable microrobots may allow their implantation to the TBI in various species in minimally invasive surgeries. This is due to the considerable variation in TBI size across different species[5]. As shown in Supplementary Fig. 5, the width of the TBI in the rotator cuff in normal rats was approximately 450 μm. In addition, the use of oversized microrobots may increase the difficulty of surgical reconstruction of RCT, while the use of undersized microrobots increases the risk of

https://doi.org/10.1038/s41467-025-57499-x

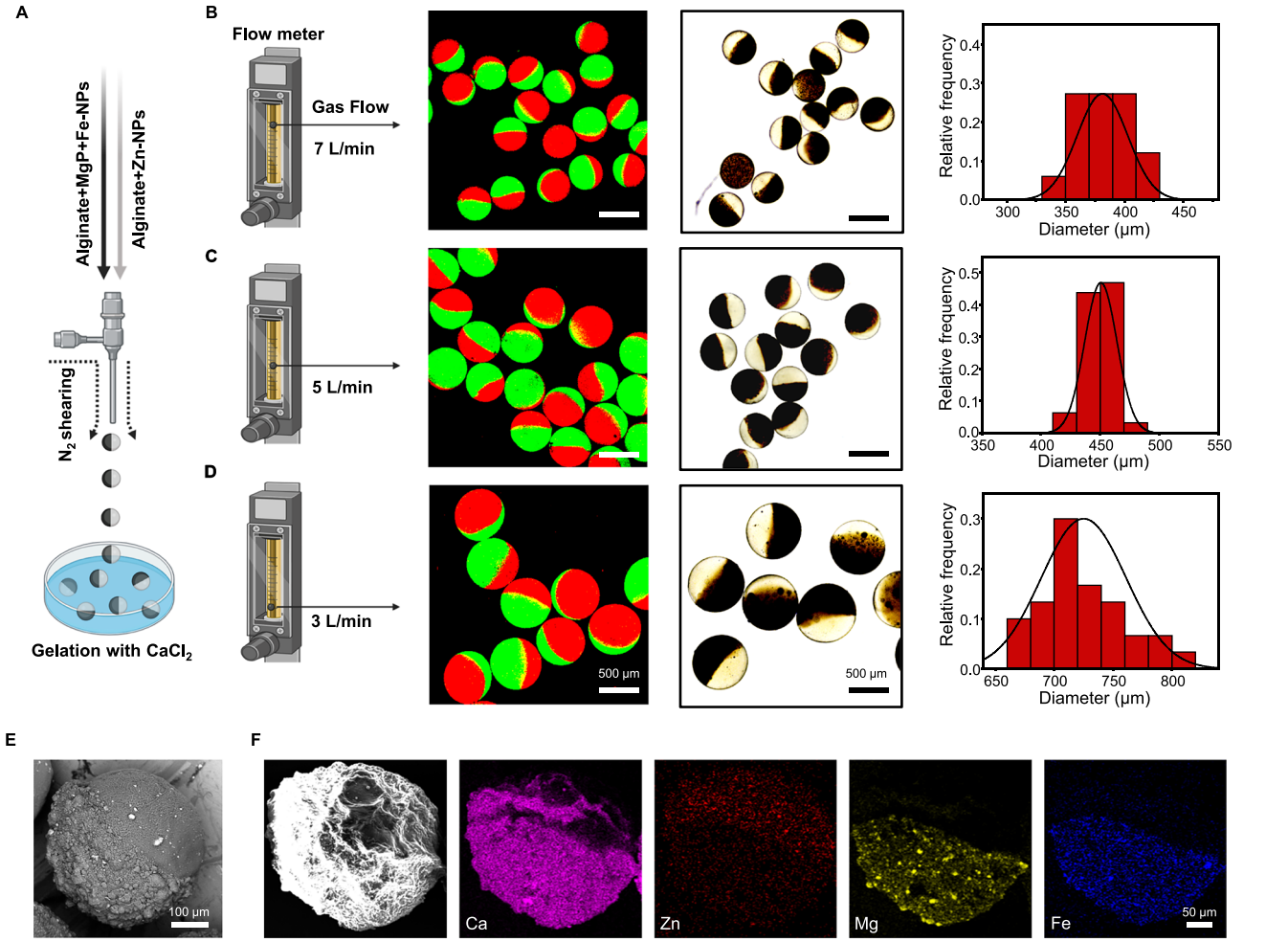

Fig. 2 | Fabrication and characterization of microrobots. A Schematic showing the microrobot fabrication process. **B**–**D** CLSM images, bright-field images, and size distributions of the microrobots prepared with various nitrogen flow rates. **E** Cryo-SEM image of microrobots. **F** SEM image (left) of microrobots and EDS images (right) of Ca (pink), Zn (red), Mg (yellow) and Fe (blue). For (**B**–**F**), experiments were repeated for 3 times independently with similar results. MgP: $Mg_3(PO_4)_2$, Fe-NPs: Fe_3O_4 nanoparticles, Zn-NPs: ZnO nanoparticles. (**A**) and left pannel of (**B**–**D**) created in BioRender. Ding, Z. (2025) https://BioRender.com/p69t917. Source data are listed in the Source Data file.

detachment from the TBI. Therefore, we finally chose the microrobots with a diameter of 450 μm for further experiments. Cryo-scanning electron microscopy (cryo-SEM) image further revealed a substantial contrast in the morphology of the two separated compartments in the microrobots, with a distinct demarcation line (Fig. 2E). Furthermore, SEM and EDS confirmed the Mg and Fe were distributed in the bone side of the microrobots while Zn was mainly distributed in the other hemisphere (Fig. 2F), showing an existing Mg^{2+}/Zn^{2+} gradient in the microrobots. Recently, hydrogel microspheres featuring complex structures such as Janus, core-shell, and multicompartment designs have gained increased attention in biomedical applications because of their enhanced capabilities and sophisticated functionalities, including drug/cell delivery, scaffold fabrication, and 3D bioprinting[38–41]. However, the fabrication technique, hydrogel prepolymer selection, and crosslinking mechanism of hydrogel microspheres often negatively affect their biocompatibility, especially for those with complex structures, thus limiting their application[42,43]. The fabrication strategy of the microrobots in this study is considered biocompatible since we apply the oil-free fabrication method and the ionic crosslinking strategy. The use of FDA-approved alginate as a building block for microrobots further promises its biocompatibility and feasibility for clinical translation. When utilized for cell encapsulation, alginate may adversely affect cellular functions, including proliferation, adhesion, and differentiation, due to a lack of intrinsic integrin binding sites[44]. Conversely, alginate presents major advantages as a delivery vehicle for bioactive agents when not employed for cell encapsulation[45], as demonstrated in this study, where it enables the controlled delivery of bioactive ions. The favorable biocompatibility and mild cross-linking methods of alginate further promote its applicability. However, it is essential to recognize that even when alginate is not used for cell encapsulation, the lack of cell-adhesive properties may negatively impact the adhesion of endogenous cells, thereby affecting the efficacy of tissue repair processes.

Motion behavior and mineral gradient rebuilding effect of microrobots

To validate the feasibility and accuracy of microrobot manipulation in RCT reconstruction surgery, the motion behavior of microrobots under a magnetic field have been investigated (Fig. 3A). A NdFeB magnet was placed approximately 2–3 cm away from the microrobots, generating a magnetic field strength of approximately 100–150 mT to control the motion of the microrobots (Supplementary Fig. 6). Microrobots can perform rotational motion and align in the same direction under the magnetic field in a Petri dish (Fig. 3B). The Fe-NPs-dispersed hemispheres provided the controllable magnetic driving force for the microrobots to rotate (Supplementary Fig. 7 and Supplementary Movie 2). An ex vivo TBI model was used to simulate the motion trajectory of microrobots in the TBI. After we placed a magnet adjacent to the bone, the bone side of the microrobots with Fe-NPs

https://doi.org/10.1038/s41467-025-57499-x

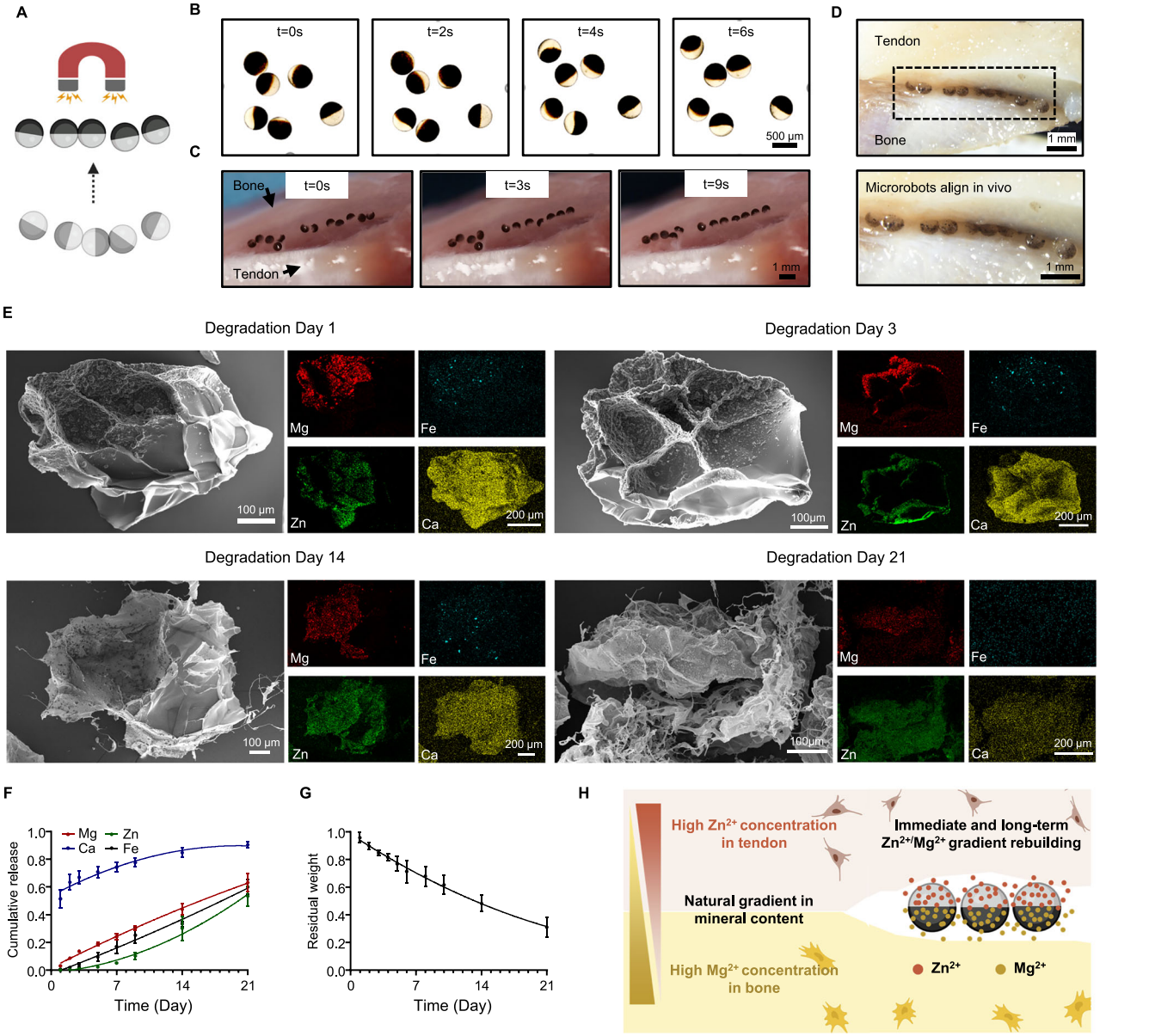

Fig. 3 | Motion behavior and mineral gradient rebuilding effect of microrobots. **A** Schematic illustration of the motion behavior of the microrobots under an external magnetic field. **B** Time-lapse images of the microrobots performing rotational motion and aligning in the same direction in a Petri dish. **C** In an ex vivo model, the bone side of the microrobots (nontransparent side) rotated and oriented toward the bone, whereas the tendon side of the microrobots (semi-transparent side) oriented toward the tendon under an external magnetic field. **D** The microrobots were aligned in an in vivo RCT model after magnetic manipulation. **E** SEM and EDS images of the microrobots on degradation days 1, 3, 14, and 21. Experiments were repeated for 3 times independently with similar results. **F** Release curve of metal ions from the microrobots. Data are presented as mean ± SD (n = 3 independent experiments). **G** Degradation profile of the microrobots. Data are presented as mean ± SD (n = 3 independent experiments). (H) Schematic illustration of the natural mineral gradient rebuilding effect of the microrobots. **A**, **H** created in BioRender. Ding, Z. (2025) https://BioRender.com/p69t917. Source data are listed in the Source Data file.

rotated and oriented toward the bone, whereas the tendon side of the microrobots oriented toward the tendon (Fig. 3C and Supplementary Movie 3). In vivo, the microrobots also showed satisfactory alignment after magnetic manipulation in an RCT model (Fig. 3D). A model equation in terms of the relationship between the size of microrobot (d) and the maximum distance between microrobot and magnet (Z) to manipulate the motion of microrobot is given below in Eq. (1):

$$d = \frac{1+\chi_m}{\chi_m}\frac{128\tau_0}{3\sin\theta}\frac{1}{\mu_0 M_0^2 R^2\left[\frac{z+l}{\left((z+l)^2+R^2\right)^{0.5}}-\frac{z}{\left(z^2+R^2\right)^{0.5}}\right]\left[\frac{1}{\left(z^2+R^2\right)^{1.5}}-\frac{1}{\left((z+l)^2+R^2\right)^{0.5}}\right]} \quad (1)$$

where χ_m is Magnetic susceptibility, μ_0 is vacuum magnetic permeability, M_0 is magnetization of the magnet, τ_0 is startup shear force, R is radius of the magnetic cylinder, L is height of the magnetic cylinder (Supplementary Fig. 8), and the derivation of the equation is shown in the supporting information[46,47]. By substituting the relevant estimated values, the relationship between d and Z is presented in Supplementary Fig. 9. The results showed that placing the magnet at a distance of 3 cm from the microrobot was sufficient to initiate rotational motion for microrobots with a diameter exceeding 200 μm.

We then assessed the concentrations of Mg^{2+} and Zn^{2+} in the bone and tendon tissues of the rotator cuff of normal rats, and the results are shown in Supplementary Table 1. The concentration of Mg^{2+} in bone is 8.7 times higher than that in tendon, while the concentration of

Zn^{2+} in tendon is 1.8 times higher than that in bone, indicating an opposing distribution trend of Mg^{2+} and Zn^{2+} and the presence of a gradient in mineral concentration in the TBI. A comparison of the data in Supplementary Table 1 and 2 revealed that the concentrations of Mg^{2+} in the bone side and Zn^{2+} in the tendon side of the microrobots were close to that in natural bone and tendon tissues, respectively. It is worth to mention that, the concentration of Mg^{2+} and Zn^{2+} loaded in Janus microrobots was not entirely determined by the natural concentration in the tissue in this study; it was also investigated by in vitro experiments. Microspheres loaded with different concentrations of MgP and Zn-NPs were cocultured with BMSCs and TCs. The results showed that the microspheres loaded with 1% MgP and the microspheres loaded with 0.1% Zn-NPs had good biocompatibility and the ability to promote cell proliferation (Supplementary Figs. 10–11); these concentrations were selected for the following experiments and their therapeutic effects were further proved in both in vitro and in vivo experiments. Given the magnetically controlled alignment behavior and Mg^{2+}/Zn^{2+} gradient of the microrobots, we can speculate that microrobots could match and rebuild the natural Mg^{2+}/Zn^{2+} gradient in the TBI immediately after implantation. Next, we investigated the long-term effect of microrobots on mineral gradient rebuilding in the TBI. The microrobots were immersed in sterile phosphate buffered saline (PBS) to simulate degradation under physiological conditions. From degradation days 1 to 21, SEM images showed that the microrobots gradually disintegrated over time, whereas the distinct morphology of the bone and tendon sides remained consistently clear. EDS mapping showed that the Mg^{2+}/Zn^{2+} content of the degraded microrobots still exhibited a gradient distribution (Fig. 3E and Supplementary Fig. 12). Zn showed a distribution trend toward the bone side, possibly due to the crosslinking of Zn^{2+} with alginate following exchange with Ca^{2+}. Notably, Fe was colocalized with Mg in the bone side of the microrobots throughout the degradation process, demonstrating a slow degradation trend of the Fe-NPs loaded in the microrobots and ensuring the post-implantation adjustability of microrobots' orientation through an external magnetic field after RCT reconstruction surgery. Notably, in the ion release experiments, the microrobots presented prolonged release curves for both Mg^{2+} and Zn^{2+} for more than 21 days (Fig. 3F). The release of Fe^{2+}/Fe^{3+} also follows a gradual release profile, which mitigates the potential toxicity (Fig. 3F). As shown in Fig. 3G, the microrobots had a slow degradation curve with a duration of retention exceeding 21 days. Given that TBI healing involves concurrent repair of soft and hard tissues and is a time-consuming process[48], the prolonged retention time and long-term ion release ensure the therapeutic efficacy of microrobots within the body. A schematic of the immediate and long-term natural Mg^{2+}/Zn^{2+} gradient rebuilding effect of microrobots is shown in Fig. 3H. Considering the complexity and precision of RCT reconstruction surgery, the use of bioactive ions-loaded microrobots with precise and noncontact manipulation properties will undoubtedly provide substantial assistance in restoring the mineral gradient of the TBI in RCT reconstruction surgery.

In vitro evaluation of the ability of Zn^{2+}-loaded microrobots to promote tendon regeneration

To demonstrate the biocompatibility of the Zn-loaded microspheres, we first constructed single-compartment alginate-Ca^{2+} microspheres (named Ms, Supplementary Fig. 13) and single-compartment microspheres loaded with Zn-NPs (named Zn-Ms). After coculturing the Zn-Ms with TCs in the Transwell system for 3 and 7 days, Live/Dead staining revealed that almost no cells died in any of the groups, with significantly more live cells in the Zn-Ms group (Fig. 4A and Supplementary Fig. 14). Consistent with the Live/Dead staining results, the results of the Cell Counting Kit-8 (CCK-8) assay showed that Zn-Ms significantly promoted the proliferation of TCs over a period of 7 days when compared to control and Ms (Fig. 4B). Comparative analysis with Ms revealed that the proliferative effect facilitated by Zn-Ms was attributed primarily to the loaded Zn^{2+}, and the results were consistent with those of previous studies[20,21]. Next, we performed Transwell chemotaxis experiments and scratch wound healing assays to evaluate the migration capacity of TCs. In the Transwell experiment, TCs in the upper chamber migrated toward the Zn-Ms in the lower chamber due to the chemotactic effect of Zn^{2+}, as indicated by more migrated cells stained with crystal violet in the Zn-Ms group than in the other groups (Fig. 4C and E). In the scratch wound healing assay, TCs in the Zn-Ms group migrated to the scratched area faster throughout the experiment in response to the Zn^{2+} released from the Zn-Ms (Fig. 4D, F and Supplementary Fig. 15). Since the migration and accumulation of seed cells in injured tissue are crucial for tissue regeneration, the TCs recruitment capacity of the Zn-Ms ensures its efficacy in the application of tendon regeneration. Throughout the tendon repair process, the early stage is characterized by the predominant production of COL-III, which results in the formation of scar-like low-strength tissue that bridges the tendon defect. Subsequently, COL-III is gradually replaced by COL-I, resulting in a more organized matrix and substantially bolstering tendon tissue strength[49–51]. As seed cells for tendon reconstruction, the functionality of TCs, primarily involving the synthesis and metabolism of collagen, significantly influences the actual outcomes of tendon repair. The COL-I/COL-III ratio determines the quality of the regenerated tendon, with a higher ratio correlating with superior results in tendon healing[49,50]. Cell immunofluorescence staining indicated that the Zn-Ms significantly increased the expression of COL-I while suppressing the expression of COL-III (Fig. 4G and Supplementary Fig. 16-17). Furthermore, the expression of tenascin-C (TNC), an important regulatory factor for tendon regeneration and remodeling[52], was upregulated in response to the release of Zn^{2+} from Zn-Ms (Fig. 4G and Supplementary Fig. 18). Consistent with the results of the immunofluorescence staining, real-time quantitative polymerase chain reaction (RT–qPCR) revealed that the Zn-Ms could upregulate COL-I and TNC mRNA expression while downregulating COL-III mRNA expression (Fig. 4H). In addition, the expression of Mohawk (MKX), a crucial tendon-specific transcription factor whose expression is positively correlated with tendon repair[53], was significantly upregulated at the transcriptional level (Fig. 4H). The ability of Zn^{2+} to regulate collagen synthesis and promote tendon formation was consistent with the findings of previous reports[20,21]. In summary, Zn-Ms promoted the proliferation, accumulation, and function of TCs, which ensured high-quality tendon reconstruction during the TBI healing process (Fig. 4I).

In vitro evaluation of the ability of Mg^{2+}-loaded microrobots to promote bone formation

Biomaterials with controlled Mg^{2+} delivery are considered highly biocompatible, and the in vitro and in vivo biological efficacy of a continuous supply of Mg^{2+} for promoting bone regeneration is promising[54]. First, we performed the Live/Dead staining and CCK-8 assays to investigate the effects of Mg-Ms on the viability and proliferation of BMSCs. The results revealed that the Mg-Ms had no cytotoxic effects on the BMSCs on days 3 and 7 (Fig. 5A and Supplementary Fig. 19) and accelerated BMSCs proliferation from days 1 to 7 (Fig. 5B). Second, since the formation of new bone requires the migration of endogenous BMSCs to the defect region, we further evaluated the effect of the Mg-Ms on the migration of BMSCs. In the Transwell experiments (Fig. 5C and Supplementary Fig. 20) and scratch wound healing assays (Fig. 5D and Supplementary Fig. 21), the Mg-Ms markedly increased the migration capacity of the BMSCs. Third, we investigated the effect of the Mg-Ms on the osteogenic differentiation of BMSCs, which is considered a fundamental property for bone regeneration. Alkaline phosphatase (ALP) staining and alizarin red staining (ARS) were performed to evaluate the osteogenic capacity of BMSCs in the early and late stages, respectively. After being induced

https://doi.org/10.1038/s41467-025-57499-x

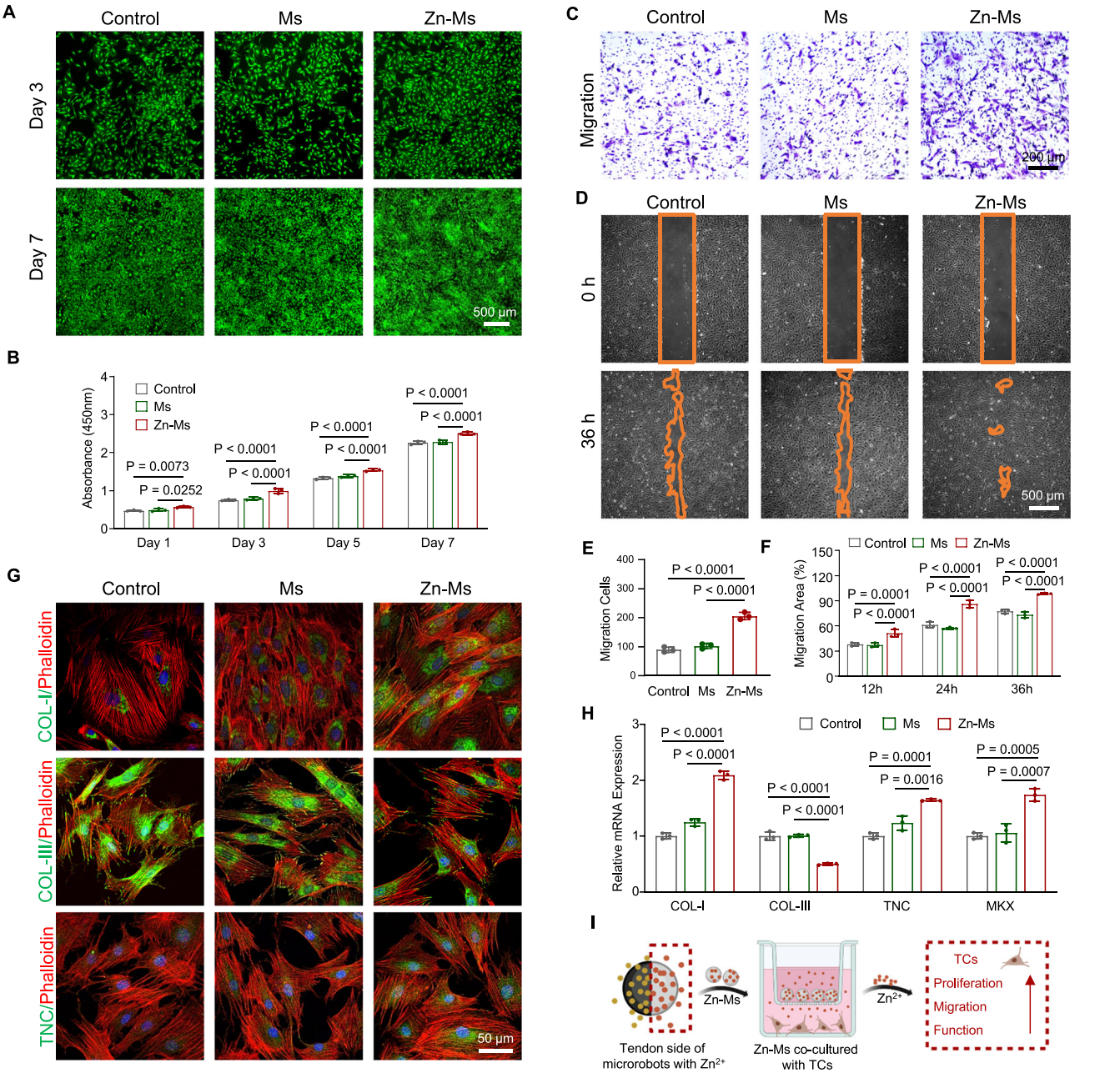

Fig. 4 | Evaluation of the ability of Zn^{2+}-loaded microrobots to promote tendon regeneration in vitro. A Live/Dead staining of TCs after coculture with the indicated microspheres for 3 and 7 days. **B** CCK-8 assay of TCs after coculture with the indicated microspheres for 1, 3, 5, and 7 days. **C** Crystal violet staining of migrated TCs in the Transwell experiment. **D** Scratch wound healing assays of TCs at 0 and 36 h. **E** Quantitative analysis of migrated TCs in the Transwell experiment. **F** Semiquantitative analysis of the migration area in the scratch wound healing assay at 12, 24, and 36 h. **G** COL-I, COL-III, and TNC immunofluorescence staining (green) of TCs. The cells were costained with DAPI (blue) and phalloidin (red). **H** The relative mRNA expression of COL-I, COL-III, TNC, and MKX in TCs. **I** Schematic illustration of Zn^{2+}-loaded microrobots promoting the proliferation, migration, and tenogenesis-related functions of TCs. Data are presented as mean ± SD (n = 3 biologically independent samples). **B**, **F** two-way ANOVA with Dunnett's multiple comparisons test and adjustment applied. **E**, **H** one-way ANOVA with Dunnett's multiple comparisons test and adjustment applied. **I** created in BioRender. Ding, Z. (2025) https://BioRender.com/p69t917. Source data are listed in the Source Data file.

with osteogenic-conditioned medium for 7 and 14 days, the BMSCs in the Mg-Ms group were stained for ALP and presented a substantially larger staining area and greater staining depth than those in the other groups were (Fig. 5E and Supplementary Fig. 22), indicating the increased ALP activity induced by Mg^{2+}. BMSCs cocultured with the Mg-Ms for 14 and 21 days were stained with ARS and likewise presented a substantially larger staining area and greater staining depth (Fig. 5F and Supplementary Fig. 23), demonstrating the highest Ca^{2+} deposition efficacy. Cell immunofluorescence staining and RT–qPCR were used to measure the expression of osteogenic markers at the protein and mRNA levels. The protein expression of BMP-2, RUNX-2, and OCN (Fig. 5G and Supplementary Figs. 24–26), three important osteogenic cytokines[55,56], was verified to be markedly increased in the Mg-Ms group by cell immunofluorescence staining. RT–qPCR revealed that the mRNA expression of BMP-2, RUNX-2, OCN, and ALP was upregulated by the Mg-Ms (Fig. 5H). BMSCs in the Ms group presented a greater osteogenic differentiation capacity than those in the control group did, which may be attributed to the Ca^{2+} contained in the microspheres[57]. Finally, to demonstrate the biocompatibility of Fe-NPs-loaded microspheres, microspheres loaded with Fe-NPs (named Fe-

https://doi.org/10.1038/s41467-025-57499-x

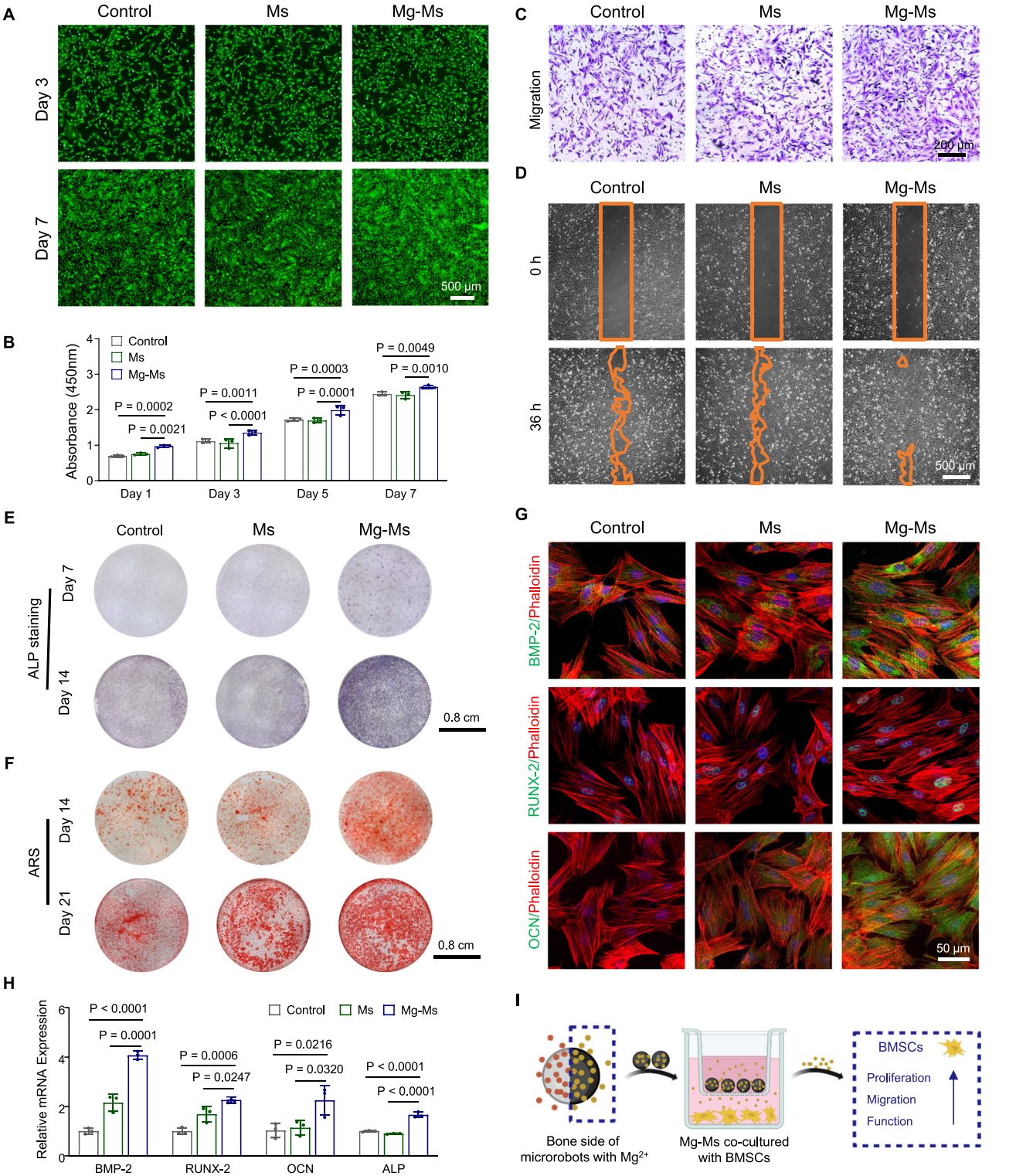

Fig. 5 | Evaluation of the ability of Mg^{2+}-loaded microrobots to promote bone formation in vitro. A Live/Dead staining of BMSCs after coculture with the indicated microspheres for 3 and 7 days. **B** CCK-8 assays of BMSCs after coculture with the indicated microspheres for 1, 3, 5, and 7 days. Data are presented as mean ± SD (n = 3 biologically independent samples, two-way ANOVA with Dunnett's multiple comparisons test and adjustment applied). **C** Crystal violet staining of migrated BMSCs in the Transwell experiment. **D** Scratch wound healing assays of BMSCs at 0 and 36 h. **E** ALP staining of BMSCs after coculture with the indicated microspheres for 7 and 14 days in osteogenic-conditioned medium. **F** ARS of BMSCs after coculture with the indicated microspheres for 14 and 21 days in osteogenic-conditioned medium. **G** BMP-2, RUNX-2, and OCN immunofluorescence staining (green) of BMSCs. The cells were costained with DAPI (blue) and phalloidin (red). **H** Relative mRNA expression of BMP-2, RUNX-2, OCN, and ALP in BMSCs. Data are presented as mean ± SD (n = 3 biologically independent samples, one-way ANOVA with Dunnett's multiple comparisons test and adjustment applied). **I** Schematic illustration of Mg^{2+}-loaded microrobots promoting the proliferation, migration, and osteogenesis of BMSCs. **I** created in BioRender. Ding, Z. (2025) https://BioRender.com/p69t917. Source data are listed in the Source Data file.

Ms) were fabricated and cocultured with BMSCs and TCs. Live/Dead staining and CCK-8 assays both showed that the Fe-Ms exhibit no significant toxicity to BMSCs (Supplementary Figs. 27–28) or TCs (Supplementary Figs. 29–30) over a period of 7 days. This result may be attributed to the slow release of Fe^{2+}/Fe^{3+} from the microspheres (Fig. 3F). In addition, the Fe-Ms and Ms were cocultured with cells to investigate the effects of Fe^{2+}/Fe^{3+}, Ca^{2+}, and their potential interactions on osteogenesis and tenogenesis. RT–qPCR revealed that Ca^{2+} promoted the osteogenic differentiation of BMSCs and the tenogenesis-related function of TCs, whereas Fe^{2+}/Fe^{3+} did not further influence this effect Supplementary Figs. 31–32). In summary, Mg-Ms promoted the proliferation, migration, and osteogenic differentiation of BMSCs, confirming the effectiveness of the bone side of the microrobots in new bone formation during TBI healing (Fig. 5I).

Overall, the in vitro studies confirmed the spatiotemporal cell phenotype modulation effect of the microrobots: the bone side of microrobots loaded with Mg^{2+} and the tendon side of microrobots loaded with Zn^{2+} continuously promoted the proliferation, migration, and function of the BMSCs and TCs, respectively, thus guaranteeing the reconstruction of the cell phenotype gradient in the TBI and orchestrating the synchronous regeneration of the tendon and bone.

Regeneration of gradient structure in rat RCT healing by microrobots

Given the great effects on Mg^{2+}/Zn^{2+} gradient rebuilding and cell phenotype modulation, Janus microrobots were applied in a rat RCT model to assess their in vivo therapeutic efficacy. The establishment of rat RCT model, microrobot implantation in RCT reconstruction surgery and postoperative examination methods at postoperative weeks 4 and 8 are shown in Fig. 6A. The rats were divided into 5 groups: the control group (suture), Mg-Ms group (suture + microspheres loaded with MgP and Fe-NPs), Zn-Ms group (suture + microspheres loaded with Zn-NPs), Mg/Zn-Mixed-Ms group (suture + microspheres loaded with mixed MgP, Fe-NPs and Zn-NPs) and Mg/Zn-Janus-Mr group (suture + Janus microrobots separately loaded with MgP & Fe-NPs or Zn-NPs). New bone formation at the greater tuberosity of the humeral head of rats was assessed by the micro-computed tomography (micro-CT). The Mg/Zn-Janus-Mr group presented a relatively continuous bone line without any defects at the humeral head when compared to other groups after 4 weeks of repair (Fig. 6B). At postoperative week 8, the Mg/Zn-Janus-Mr group presented a relatively integrated greater tuberosity of the humeral head, similar to the normal anatomy, suggesting promoted bone formation at the repair area (Fig. 6B and Supplementary Fig. 33). A 7T animal magnetic resonance imaging (MRI) system was used to evaluate the tendon regeneration status in vivo. At postoperative week 4, the supraspinatus tendon in the control, Mg-Ms, Zn-Ms, and Mg/Zn-Mixed-Ms groups presented high signal intensity, with the highest signal intensity in the control group, indicating severe edema and inflammation in the tendons. In contrast, the Mg/Zn-Janus-Mr group showed a significantly lower signal intensity in the tendon (Fig. 6C). At postoperative week 8, the tendon in the Mg/Zn-Janus-Mr group presented a relatively continuous signal with the lowest intensity among all groups, similar to that of a normal tendon, suggesting promotion of tendon regeneration by the microrobots (Fig. 6C and Supplementary Fig. 34). Given that we observed bone formation and tendon regeneration in the rats with RCT, we further assessed the strength of the repaired TBI tissue through a biomechanical test (Supplementary Fig. 35). While the mechanical properties of TBI tissue, including the maximum load and stiffness, tended to increase over time in all groups, the strength of the TBI tissue in the Mg/Zn-Janus-Mr group was the highest among the groups and notably increased from postoperative weeks 4 to 8 (Fig. 6D, E). This promotion can be attributed to the gradient structure of the TBI regenerated by the microrobots, which is crucial for effectively distributing stress loads[5,6], despite RCT surgery being capable of re-establishing the continuity of the TBI. Since functional recovery after surgery is the most crucial issue for RCT patients from a clinical perspective, gait analysis was conducted to analyze the function of the forelimb in the rats with RCT[58,59]. The gait assessment by collecting rat pawprints at postoperative weeks 4 and 8 was accomplished by measuring the stride length and step length, as shown in Supplementary Fig. 36. Compared with those in the other groups, the stride length and step length in the Mg/Zn-Janus-Mr group significantly recovered at weeks 4 and 8 (Fig. 6F–H). In summary, microrobots can induce new bone formation and tendon regeneration simultaneously and promote the regeneration of gradient tendon–bone transition structures in the TBI. The augmentation of TBI healing is evident not only in the mechanical properties but also in the restoration of limb function, with anticipated positive outcomes for clinical patients.

To directly evaluate the regenerated gradient structure of TBI, we examined the histology of regenerated TBI with Hematoxylin Eosin (HE), Masson, and Sirius Red staining. At postoperative week 4, TBI healing in the control group was poor and delayed, with immature granulation tissue connecting the damaged tendon and bone. Newly formed bone at the footprint of the greater tuberosity was relatively mature in the Mg-Ms group, suggesting the enhanced and accelerated new bone regeneration by Mg^{2+}. In the Zn-Ms group, presence of tendon-like cells can be observed with relatively organized collagen fibers and collagen matrix deposition. The Mg/Zn-Mixed-Ms group had a more regular morphology and arrangement of the tendon tissue, but the gradient structure of TBI had not yet recovered. Compared with the other groups, the Mg/Zn-Janus-Mr group presented mature bone formation that was structurally integrated well with the regenerated tendon, where denser and well-oriented collagen can be found (Fig. 7A). Using a modified histological scoring system, we evaluated the regeneration of tendon and bone as well as the restoration of the tendon–bone transition structure. At postoperative week 4, the Mg/Zn-Janus-Mr group had significantly higher scores than the other groups did (Fig. 7B, C). Compared with those at week 4, all the groups showed progressive repair at week 8, manifesting as fewer infiltrating inflammatory cells as well as more organized and thicker collagen fibers. The Mg/Zn-Janus-Mr group demonstrated of the synergistic effect of promoted bone repair induced by Mg^{2+} and accelerated tendon regeneration induced by Zn^{2+} and presented a distinct gradient structure of tendon–bone transition with an apparent tidemark, which was similar to the natural TBI structure (Fig. 7D, Supplementary Fig. 5 and Supplementary Fig. 37). The modified scoring system also revealed that the Mg/Zn-Janus-Mr group had the highest score among all the groups at week 8, indicating promotion of TBI healing and a regenerated gradient structure incorporating tendon maturity and bone formation (Fig. 7E, F).

The underlying mechanisms of osteogenesis induced by the microrobots were analyzed by performing multiplex immunofluorescence. BMP-2, a crucial osteogenic factor primarily expressed by BMSCs, plays a critical role in bone regeneration during TBI healing[60,61]. BMP-2 expression was observed at the repaired TBI in this study (Supplementary Fig. 38). As shown in Fig. 8A of magnified views, the Mg/Zn-Janus-Mr group presented the highest signal intensity and the broadest distribution of the BMP-2 protein among all the groups. Semiquantitative analysis also confirmed that the proportion of cells expressing BMP-2 was the highest in the Mg/Zn-Janus-Mr group at postoperative weeks 4 and 8 (Fig. 8B and D). Comparisons of the Mg-Ms group with the control and Zn-Ms groups suggested that high-level osteogenesis was maintained by Mg^{2+}, which is consistent with a previous report[62]. At postoperative week 8, all groups exhibited a slight decrease in BMP-2 signal intensity, demonstrating that BMP-2 expression was activated in the early phase of TBI healing, which was consistent with previous reports[61,62]. OCN is another important osteogenic marker that is expressed mainly in the later phase of bone formation[25,63]. Positive staining of OCN in the Mg/Zn-Janus-Mr group

https://doi.org/10.1038/s41467-025-57499-x

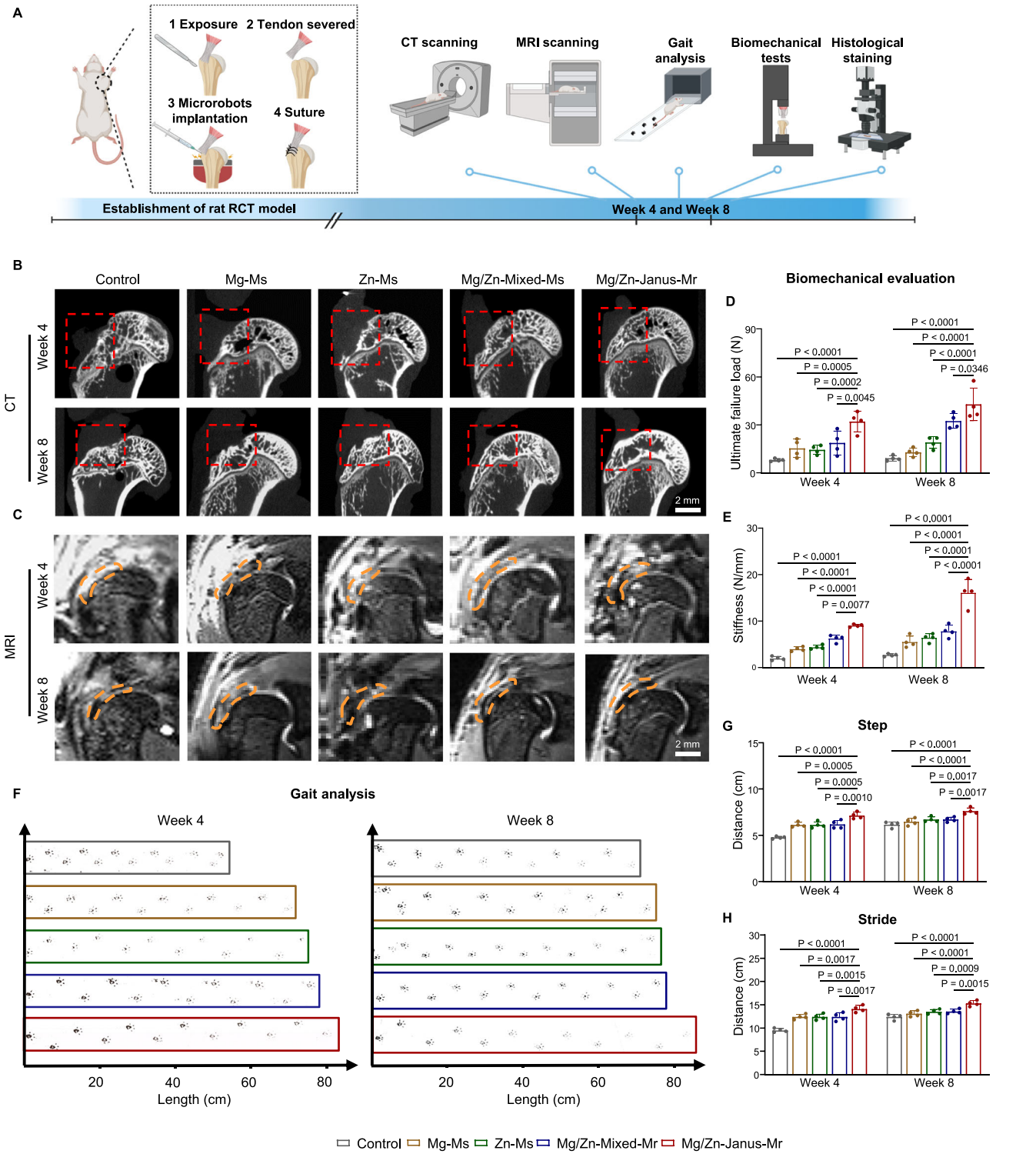

Fig. 6 | Radiological evaluation, biomechanical test, and gait assessment of the rat RCT model. A Schematic illustration of the establishment of the rat RCT model, the implantation of microrobots in RCT reconstruction surgery, and the post-operative examination methods. **B** Micro-CT images of the humeral head used to assess new bone formation at postoperative weeks 4 and 8. **C** MRI images of the supraspinatus–humerus complex used to assess tendon regeneration at post-operative weeks 4 and 8 in vivo. **D**, **E** Biomechanical evaluation of TBI tissue at postoperative weeks 4 and 8. Data are presented as mean ± SD (n = 4 biologically independent samples, two-way ANOVA with Dunnett's multiple comparisons test and adjustment applied). **F** Gait analysis of rats with RCT to assess forelimb functional recovery at postoperative weeks 4 and 8, and (**G**, **H**) corresponding quantitative analyses of stride length and step length. Data are presented as mean ± SD (n = 4 biologically independent samples, two-way ANOVA with Dunnett's multiple comparisons test and adjustment applied). RCT: rotator cuff tear, CT: computed tomography, MRI: magnetic resonance imaging. **A** created in BioRender. Ding, Z. (2025) https://BioRender.com/p69t917. Source data are listed in the Source Data file.

https://doi.org/10.1038/s41467-025-57499-x

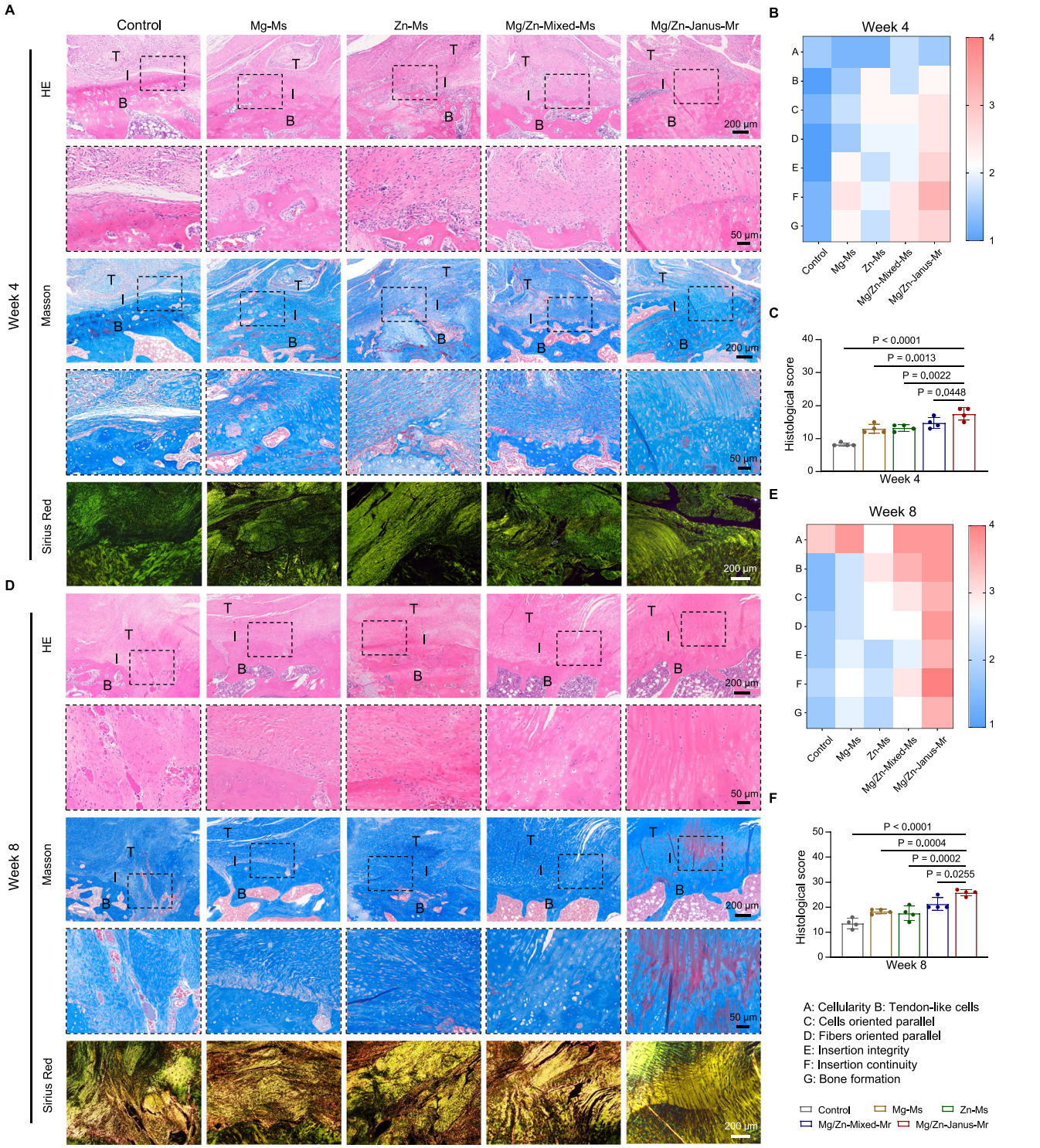

Fig. 7 | Histological evaluation of the regenerated TBI. A Histological images of the regenerated TBI and enlarged views of HE, Masson, and Sirius red staining at postoperative week 4. **B** Heatmap showing the specific score for each item of the modified histological scoring system among the different groups, and (**C**) corresponding quantitative analyses of the histological scores at postoperative week 4. Data are presented as mean ± SD (n = 4 biologically independent samples, one-way ANOVA with Dunnett's multiple comparisons test and adjustment applied). **D** Histological images and enlarged views at postoperative week 8. **E** Heatmap scores, and (**F**) corresponding quantitative analyses at postoperative week 8. Data are presented as mean ± SD (n = 4 biologically independent samples, one-way ANOVA with Dunnett's multiple comparisons test and adjustment applied). Source data are listed in the Source Data file.

was significantly higher than that in any other group (Fig. 8A). Quantitative analysis confirmed that the proportion of cells expressing OCN was higher in the Mg/Zn-Janus-Mr group at postoperative weeks 4 and 8 (Fig. 8C and E). To evaluate the collagen type and matrix deposition during the tendon regeneration process, the immunofluorescence staining for COL-I and COL-III was performed. In addition, the tenogenic marker TNC was costained to assess tenogenic activity. The Mg/Zn-Janus-Mr group exhibited contrasting results for COL-I and COL-III: microrobots promoted the expression and deposition of COL-I but suppressed those of COL-III (Fig. 8F). Semiquantitative analysis

https://doi.org/10.1038/s41467-025-57499-x

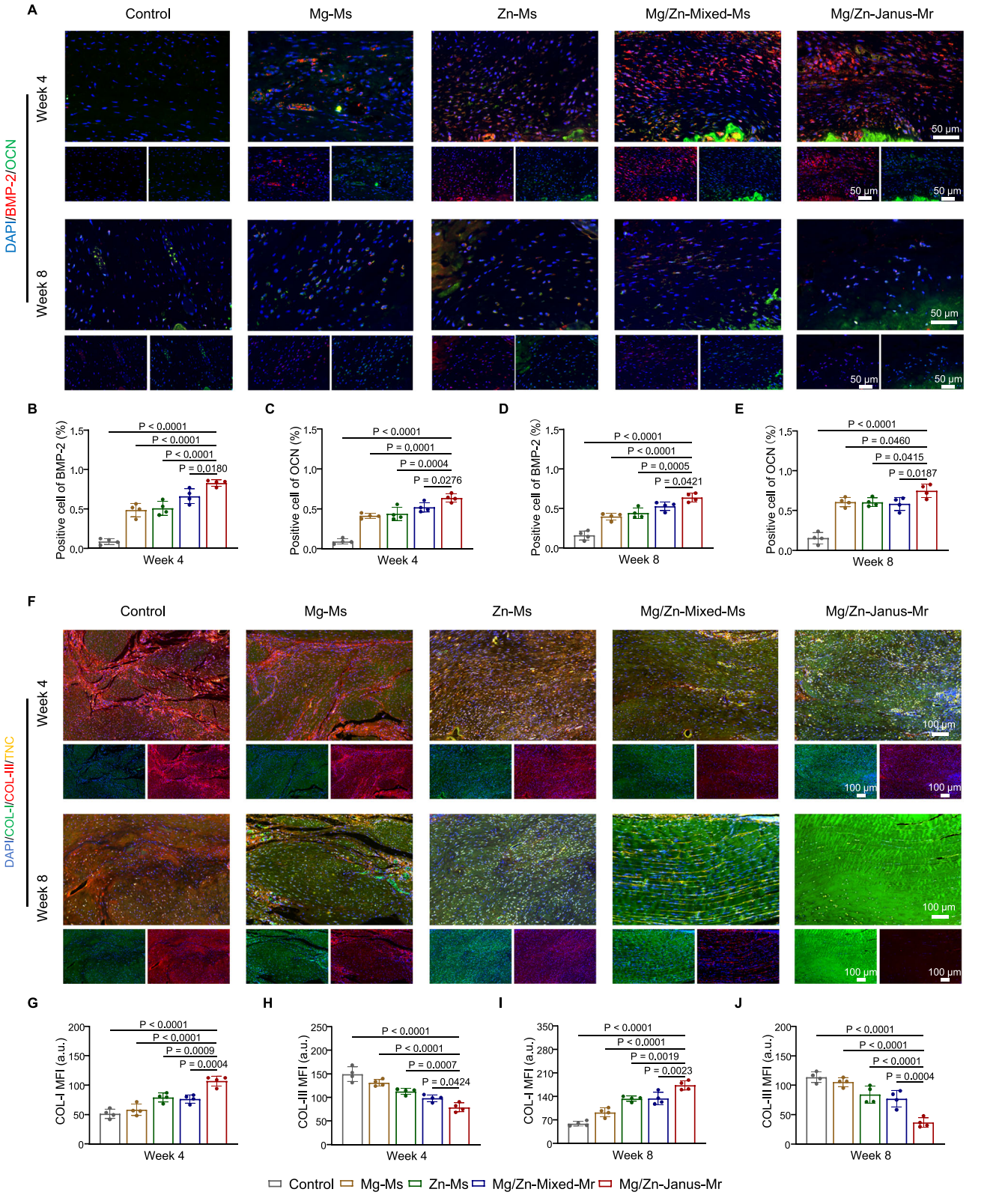

Fig. 8 | The underlying mechanisms of osteogenesis and tenogenesis induced by the microrobots analyzed by multiplex immunofluorescence. A Multiplex immunofluorescence of osteogenic markers in regenerated TBI tissue at post-operative weeks 4 and 8: BMP-2 (red) and OCN (green). The cells were costained with DAPI (blue) to visualize the nuclei. Upper panel: merged images; lower panel: split images. **B** Quantitative analyses of BMP-2-positive cells in the TBI region at postoperative week 4. **C** Quantitative analyses of OCN-positive cells in the TBI region at week 4. **D** Proportion of BMP-2-positive cells at postoperative week 8. **E** Proportion of OCN-positive cells at postoperative week 8. **F** Multiplex immunofluorescence of the regenerated tendon for COL-I (green), COL-III (red), and TNC (yellow). The cells were costained with DAPI (blue) to visualize the nuclei. Upper panel: merged images; lower panel: split images for COL-I and COL-III. **G** Quantitative analyses of the COL-I mean fluorescence intensity (MFI) at post-operative week 4. **H** Quantitative analyses of the COL-III MFI at postoperative week 4. **I** MFI of COL-I at postoperative week 8. **J** MFI of COL-III at postoperative week 8. a.u., arbitrary units. Data are presented as mean ± SD (n = 4 biologically independent samples, one-way ANOVA with Dunnett's multiple comparisons test and adjustment applied). Source data are listed in the Source Data file.

confirmed these results throughout the repair process (Fig. 8G–J). Furthermore, more organized and oriented collagen fibers could be easily observed in the Mg/Zn-Janus-Mr group during the TBI healing process (Fig. 8F). Positive staining of TNC was significantly higher in the Mg/Zn-Janus-Mr group than in the other groups, demonstrating the promotion of TCs function (Fig. 8F and Supplementary Figs. 39–40). As a result, we speculate that the microrobots successfully reconstructed the matrix components and stimulated the function of TCs[64,65]. A comparison of the results between the Zn-Ms group and the control group as well as the Mg-Ms group revealed that Zn^{2+} has a therapeutic effect on tendon regeneration. Additionally, in a comparison of the results between the Mg/Zn-Janus-Mr group and the Mg/Zn-Mixed-Ms group, the Zn^{2+} gradient induced by the Janus structure of the microrobots significantly enhanced the therapeutic efficacy of Zn^{2+}. In summary, the in vivo mechanism by which microrobots promoted TBI healing was attributed to the promotion of osteogenesis and tenogenesis by the mineral gradient, with early osteogenesis being mediated by BMP-2 and late osteogenesis being modulated by OCN and tenogenesis being reflected in matrix reconstruction and TCs function stimulation.

Immunomodulatory effects of microrobots during TBI healing

An appropriate inflammatory response can facilitate early TBI healing; however, excessive and prolonged inflammation can severely impair and disrupt TBI healing, leading to the formation of pathological scar tissue[66,67]. Owing to the absence of natural gradients, TBI repaired with scar tissue often exhibit poor mechanical strength and biological function, increasing susceptibility to retearing and failure[68]. In the inflammatory response during TBI healing, the accumulation and phenotype alteration of macrophages play crucial roles and have garnered increased attention[69–72]. In previous studies, immunomodulatory biomaterials with the ability to scavenge reactive oxygen species (ROS) could reduce M1 macrophage accumulation and induce M2 macrophage polarization in TBI and thus achieve optimized tissue repair outcomes[66,72–74]. Here, the immunomodulatory effect of microrobots was determined by coculturing the microspheres with lipopolysaccharide (LPS)-stimulated RAW 264.7 cells. The intracellular ROS of the macrophages were assessed with 2′,7′-dichlorofluorescein diacetate (DCFH-DA), and the results revealed that the microrobots effectively scavenged the intracellular ROS (Fig. 9A, B). The anti-ROS effect demonstrated in the Mg-Ms and Zn-Ms groups indicated that the ROS-scavenging ability of the microrobots was attributed to the synergistic effects of the released Mg^{2+} and Zn^{2+}. The polarization of macrophages was investigated through immunofluorescence staining of M1 macrophage-specific markers (iNOS and CD86) and an M2 macrophage surface marker (CD206). All three microspheres effectively weakened the fluorescence signals of iNOS and CD86 and strengthened the signaling of CD206, with the microrobots producing the strongest effect (Fig. 9C–F). Similar results were obtained in RT-qPCR experiments. The mRNA expression levels of M1 macrophage markers (TNF-α and CD86) were markedly downregulated, whereas those of the M2 macrophage marker (CD206) were upregulated in the Mg-Ms, Zn-Ms and Mg/Zn-Janus-Mr groups, while the Mg/Zn-Janus-Mr group presented superior results compared with those of the Mg-Ms and Zn-Ms groups (Fig. 9G). These results verified that the microrobots inhibited M1 polarization and promoted M2 polarization of the macrophages through the synergistic ROS-scavenging effect of Mg^{2+} and Zn^{2+} (Fig. 9H). The in vivo immunomodulatory effect was evidenced by immunofluorescence staining of CD86 and CD206 in the rat regenerated TBI after 4 weeks of RCT reconstruction surgery (Fig. 9I). An abundance of CD86-positive cells was found in the control group, suggesting the occurrence of inflammatory responses after surgery. Intervention with Mg-Ms or Zn-Ms significantly decreased the number of CD86-positive cells and increased the number of CD206-positive cells. Importantly, the Mg/Zn-Janus-Mr group had the lowest CD86-positive cell ratio among the groups (Supplementary Fig. 41), and CD206-positive cells became the dominant macrophage phenotype (Supplementary Fig. 42). These results suggest that the transformation of the immune microenvironment from proinflammatory to proresolving during TBI healing was triggered through the immunomodulatory effects of the microrobots. Previous studies have also reported the roles of Mg^{2+} in the healing of the TBI[73,74] and of Zn^{2+} in the healing of tendon[20] and bone[60], specifically regarding their anti-inflammatory effects and their ability to modulate the macrophage phenotype. This study further confirms the synergistic immunomodulatory effects of these two bioactive ions in promoting TBI healing facilitated by microrobots. Overall, microrobots with immunomodulatory effects scavenge ROS, reduce M1 macrophage accumulation, and induce M2 macrophage polarization in vitro and in vivo, thus providing a prohealing immune environment for TBI reconstruction.

In conclusion, using a biofriendly gas-shearing microfluidic platform, we fabricated magnetic Janus hydrogel microrobots, which can play a crucial role in the regeneration of TBI gradients in RCT reconstruction surgery. The microrobots facilitated the immediate restoration and long-term maintenance of the natural mineral gradient in TBI and hence reconstructed the BMSCs/TCs cell phenotype gradient. The in vivo mechanism underlying the promotion of TBI healing induced by microrobots was attributed to accelerated osteogenesis and tenogenesis, with the more crucial aspect being the gradient tendon–bone transition structure formed during both regeneration processes. Microrobots with immunomodulatory effects can regulate macrophage polarization in vitro and in vivo, further providing a prohealing immune microenvironment for TBI reconstruction. Overall, magnetic Janus microrobots provide an effective strategy for the regeneration of the composition, cell phenotype, and structural gradient of the TBI and offer a reliable and promising approach for promoting TBI healing in RCT reconstruction surgery. In addition, this study provides an alternative strategy to fabricate Janus-structured materials for gradient tissue repair.

Methods

Materials

The following materials were used in this study: alginate (A2033, Sigma–Aldrich), $Mg_3(PO_4)_2$ (M341105, Aladdin), Fe_3O_4 nanoparticles (XFJ119, XFNANO), ZnO nanoparticles (Z112848, Aladdin), $CaCl_2$ (C299717, Aladdin), fluorescent polystyrene nanoparticles (200 nm, Xi'an Ruixi), PBS (HyClone), fetal bovine serum (Gibco), penicillin–streptomycin (Gibco), α-MEM (Gibco), DMEM (Gibco), type I collagenase (1904, BioFroxx), Transwell chambers (Labselect), Calcein/PI staining kit (C2015M, Beyotime), Cell Counting Kit-8 (K009, ZETA Life), crystal violet dye (C0121, Beyotime), ALP stain (C3206, Beyotime), ARS (ALIR-10001, OriCell), confocal dishes (15 mm, glass bottom, NEST), Eastep™ Super Total RNA Extraction Kit (LS1040, Promega), Hifair® III 1st Strand cDNA Synthesis SuperMix for qPCR Kit (11141ES10, Yeasen), SYBR Green (11184ES, Yeasen), LPS (ST1470, Beyotime), DCFH-DA (S0033S, Beyotime) and TSA kit (NEL861001KT, Akoya). The following antibodies were used for cells: anti-BMP-2 (A0231, ABclonal), anti-RUNX-2 (A2851, ABclonal), anti-OCN (A6205, ABclonal), anti-COL-I (A1352, ABclonal), anti-COL-III (A0817, ABclonal), anti-TNC (A18156, ABclonal), anti-iNOS (A3774, ABclonal), anti-CD86 (13395-1-AP, Proteintech), anti-CD206 (A21014, ABclonal), goat anti-rabbit IgG (AF 488, AS073, ABclonal), rhodamine-phalloidin (C2207S, Beyotime) and DAPI (C1005, Beyotime). The following antibodies were used for the paraffin sections: anti-BMP-2 (ab214821, Abcam), anti-RUNX-2 (ab236639, Abcam), anti-OCN (sc-365797, Santa Cruz), anti-COL-I (ab34710, Abcam), anti-COL-III (ab7778, Abcam), anti-TNC (A18156, ABclonal), anti-CD206 (24595, CST) and anti-CD86 (ab238468, Abcam).

https://doi.org/10.1038/s41467-025-57499-x

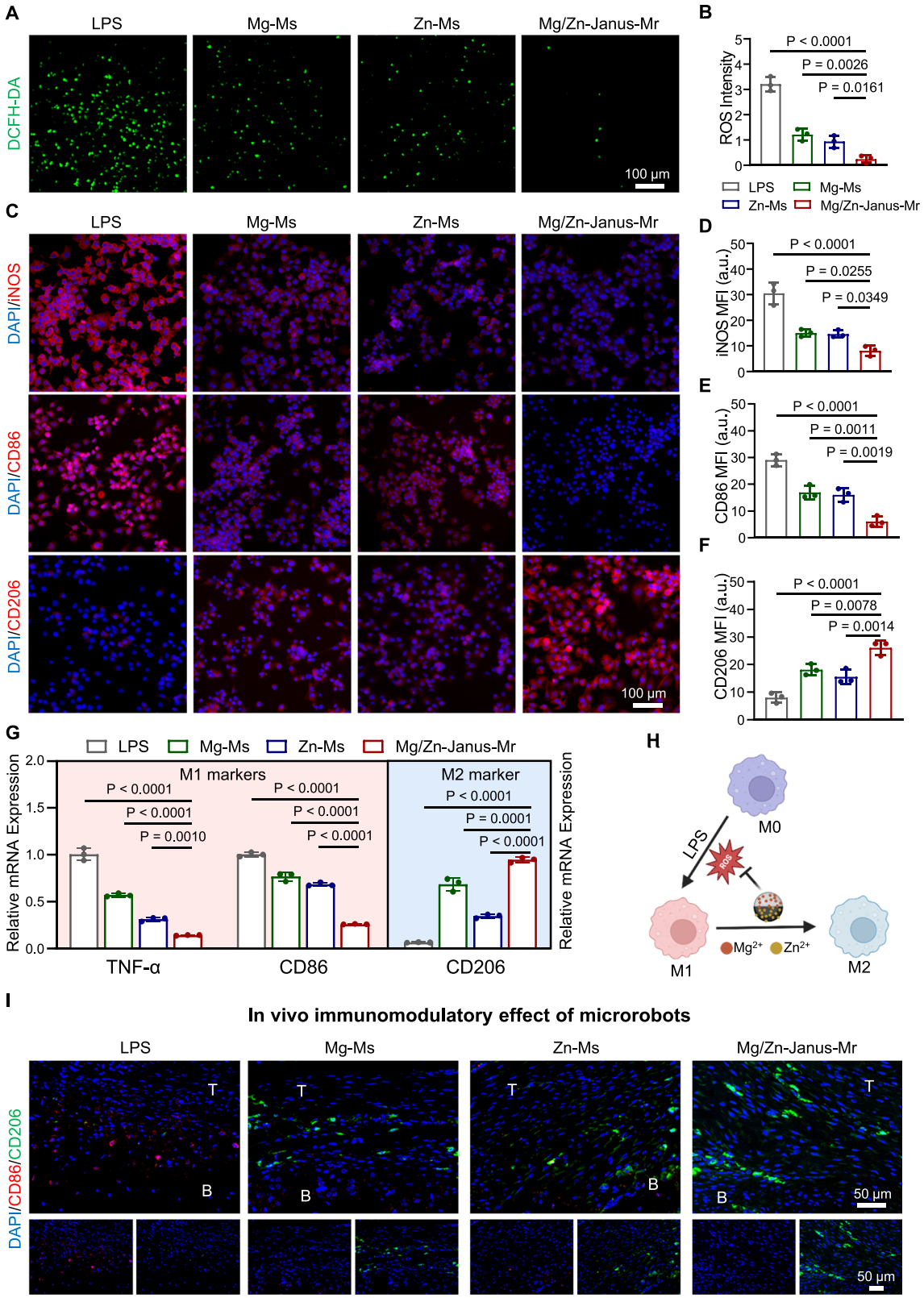

Fig. 9 | Immunomodulatory effects of microrobots during TBI healing. A DCFH-DA staining of intracellular ROS in LPS-stimulated macrophages. **B** Semiquantitative analysis of the MFI of ROS. **C** iNOS, CD86, and CD206 immunofluorescence staining (red) of LPS-stimulated macrophages. The cells were costained with DAPI (blue) to visualize the nuclei. **D**–**F** Semiquantitative analysis of the MFI of iNOS, CD86, and CD206. a.u., arbitrary units. **G** The relative mRNA expression of TNF-α, CD86, and CD206 in LPS-stimulated macrophages. **H** Schematic illustration of the immunomodulatory effect of microrobots. Microrobots inhibited M1 polarization and promoted M2 polarization of macrophages through the synergistic ROS-scavenging effect of Mg^{2+} and Zn^{2+}. **I** In vivo, CD86 (red) and CD206 (green) immunofluorescence staining of the rat regenerated TBI after 4 weeks of RCT reconstruction surgery. Upper panel: merged images; lower panel: split images. Data are presented as mean ± SD (n = 3 biologically independent samples, one-way ANOVA with Dunnett's multiple comparisons test and adjustment applied). **H** created in BioRender. Ding, Z. (2025) https://BioRender.com/p69t917. Source data are listed in the Source Data file.

Characterization of the loaded nanoparticles

The morphological structures of the Fe-NPs and Zn-NPs were observed by SEM and TEM. The elemental distributions of the Fe-NPs and Zn-NPs were detected by EDS. DLS was used to analyze the particle sizes of the Fe-NPs and Zn-NPs. XRD was used to investigate the crystal structures and crystallinities of the Fe-NPs and Zn-NPs. The magnetic characterization of the Fe-NPs was evaluated with VSM, with applied magnetic field curves from −20000 Oe to 20000 Oe.

Equipment

The gas-shearing microfluidic platform mainly consists of four parts (Supplementary Fig. 3): an electronic syringe pump for providing alginate solution; a nitrogen cylinder supplying nitrogen gas, regulated by a flowmeter to control the nitrogen flow rate; a custom-made dual-channel coaxial needle system, with two inner 30 G needles inserted in an outer needle for transporting liquids and a 14 G needle inserted in the outer needle for transporting nitrogen gas; and a collection bath containing $CaCl_2$ solution.

Fabrication of Janus hydrogel microrobots

For the fabrication of the microrobots, 1% (w/v) MgP + 0.2% (w/v) Fe-NPs or 0.1% (w/v) Zn-NPs were mixed with 2.5% (w/v) alginate and pumped into the different liquid transporting channels. The flow rate of alginate was set at 1 ml/h. Nitrogen gas was transported into the outer needle to provide a shearing force for the formation of microdroplets. The flow rate of nitrogen gas was set from 3 L/min to 7 L/min to control the size of the microrobots. Two percent (w/v) $CaCl_2$ was used in the collection bath to crosslink the alginate.

Characterization of Janus hydrogel microrobots

For visualization of the two compartments in microrobots with different diameters, 0.2% (w/v) fluorescent polystyrene nanoparticles (red and green) were added to the alginate solution, and the microrobots were observed under CLSM and inverted fluorescence microscopy. The morphology and size of the microrobots were also observed under inverted light microscopy. Cryo-SEM was used to observe the morphological structure of the microrobots. SEM and EDS were used to analyze the morphology and composition of the lyophilized microrobots. A NdFeB magnet was used to generate a magnetic field to control the motion of the microrobots. The generated magnetic field was detected using a Gaussmeter, and a computational simulation of the magnetic field was performed using COMSOL Multiphysics software. A model equation in terms of the relationship between d and Z to manipulate the motion of microrobot has been derived and the derivation processes was showed in supplementary information. The motion behavior of the microrobots was evaluated in a dish and in an ex vivo TBI model made of rat Achilles tendon and tibia. The in vivo alignment of microrobots in the TBI was evaluated in a rabbit RCT model: microrobots were implanted between the supraspinatus tendon and greater tuberosity of the humerus, and a magnet was placed on the humeral side to control the motion of the microrobots. The supraspinatus–humerus complex was then carefully harvested to observe the orientation of the microrobots. The establishment of the RCT model is described later. For the degradation and metal ion release tests, 200 mg microrobots were incubated in 2 ml of sterile PBS and agitated in a shaker at 80 rpm at 37 °C. The supernatants were changed every 2 days. At specified time points, the concentrations of four metal elements in the supernatants were examined via inductively coupled plasma–optical emission spectrometry (ICP–OES). The microrobots were weighed to calculate the residual weight (%) and then collected for SEM and EDS observation.

Primary TCs and BMSCs isolation

Primary TCs were isolated from the Achilles tendons of 8-week-old male Sprague–Dawley (SD) rats. After being washed with PBS containing 2% penicillin–streptomycin three times, the Achilles tendon was minced and fully digested in DMEM supplemented with 3 mg/ml type I collagenase at 37 °C for 45 min. After enough DMEM was added to stop digestion, the medium was filtered through a 70-μm membrane filter and centrifuged at 200 g for 4 min. Then, the TCs were resuspended and cultured in DMEM supplemented with 10% FBS and 1% penicillin–streptomycin. The TCs were passaged at 80% confluence, and passage 3 TCs were used for subsequent experiments.

Primary BMSCs were isolated from 7-day-old male neonatal SD rats. Briefly, the femurs and tibias were harvested and washed with PBS supplemented with 2% penicillin–streptomycin three times. The proximal and distal metaphysis were carefully removed from the femurs and tibias, and α-MEM was injected via a syringe to rinse the bone cavity. After the collected medium was centrifuged at 200 g for 4 min, the BMSCs were resuspended and cultured in fresh α-MEM supplemented with 10% FBS and 1% penicillin–streptomycin. Passage 3 BMSCs were used for subsequent experiments.

Biocompatibility and proliferation assays

The biocompatibility of microrobots with TCs and BMSCs was investigated by Live/Dead staining assay. TCs were seeded into the lower Transwell chambers of a 12-well plate, while Zn-Ms were placed in the upper chambers (0.4 μm pores). The BMSCs were cocultured with Mg-Ms as described above. The cells were cocultured with the Fe-Ms to investigate the biocompatibility of the Fe-Ms. After 3 and 7 days, the cells were stained with Calcein/PI staining kit for 30 min, after which live cells in green and dead cells in red were observed by an inverted fluorescence microscopy.

CCK-8 assays were used to investigate the proliferation of cells with microrobots. TCs were seeded into the lower Transwell chambers (0.4 μm pores) of a 24-well plate at a density of 1.5×10^4/well, while Zn-Ms were placed in the upper chambers. The BMSCs were cocultured with Mg-Ms as described above. The proliferation of cells cocultured with Fe-Ms was also investigated. After 1, 3, 5, and 7 days, the cells were incubated with 10% CCK-8 solution for 1 hour at 37 °C. The OD450 values were recorded with a microplate reader.

Cell migration assays

Cell migration was evaluated using Transwell and scratch wound healing experiments. For the Transwell experiments, TCs were seeded into the upper Transwell chambers (8.0 μm pores) of a 24-well plate at a density of 1×10^4/well after being subjected to serum starvation, and Zn-Ms were placed in the lower chambers. The lower chambers contained medium supplemented with 10% FBS, and the upper chambers contained medium supplemented with 1% FBS. The BMSCs were cocultured with Mg-Ms as described above. After the cells and microspheres were cocultured for 12 hours, the unmigrated cells were removed, and the migrated cells on the membranes were fixed with 4% paraformaldehyde, stained with crystal violet dye and observed under an inverted light microscope.

For the scratch wound healing experiment, TCs were seeded into the lower Transwell chambers (0.4 μm pores) of a 12-well plate to reach 100% confluency. A straight scratch line was then made on the TCs with a 200 μl pipette tip. After the cells were washed with PBS to remove the cell debris and filled with medium supplemented with 1% FBS in the lower chambers, Zn-Ms were added to the upper chambers. The BMSCs were cocultured with Mg-Ms as described above. Wound closure was recorded at 0, 12, 24, and 36 h under an inverted light microscope, and the migration area was measured using ImageJ software.

ALP staining and ARS

ALP staining and ARS were used to evaluate the effects of Mg-Ms on the osteogenic differentiation of BMSCs. Briefly, BMSCs and Mg-Ms were cocultured in a Transwell system (0.4 μm pores) with osteogenic-conditioned medium (α-MEM with 10% FBS, 1% penicillin–streptomycin, 10 mM β-glycerophosphate, 10 nM dexamethasone and 50 μg/ml ascorbic acid). After 7 and 14 days, ALP staining solution was added to each well, and the samples were incubated for 40 min at room temperature to measure the activity of ALP. After 14 and 21 days, the ARS solution was added to the well and incubated for 30 min to stain the mineralized nodules. The staining of the wells was recorded with a digital camera.

Cell immunofluorescence staining

After the BMSCs and Mg-Ms were cocultured in a Transwell system (0.4 μm pores) with osteogenic-conditioned medium for 7 days, the BMSCs were digested and seeded in confocal dishes. After adhering to the dishes, the cells were washed with PBS and fixed with 4% paraformaldehyde for 15 min. Then, the cells were blocked with 5% goat serum for 15 min and permeabilized with 0.5% Triton X-100 for 20 min. Primary antibodies against BMP-2, RUNX-2, and OCN were added and incubated overnight at 4 °C. After washed with PBS, goat anti-rabbit IgG was added, and the samples were incubated for 1 hour at 37 °C in the dark. The cytoskeleton and nucleus were counterstained with rhodamine-phalloidin and DAPI, respectively. TCs were cocultured with Zn-Ms and stained with COL-I, COL-III, and TNC using the same protocol described above. The cell immunofluorescence staining was observed using CLSM, and the MFI was analyzed via ImageJ.

RT–qPCR

After the BMSCs and Mg-Ms were cocultured in a Transwell system (0.4 μm pores) with osteogenic-conditioned medium for 7 days, the mRNA of the cells was extracted using the Eastep™ Super Total RNA Extraction Kit according to the manufacturer's instructions. The mRNA was then reverse transcribed into complementary DNA using the Hifair® III 1st Strand cDNA Synthesis SuperMix for qPCR Kit. RT–qPCR was carried out for BMP-2, RUNX-2, OCN, and ALP using gene-specific primers and SYBR Green on QUANTSTUDIO3 (Applied Biosystems). TCs were cocultured with Zn-Ms and RT–qPCR was carried out for COL-I, COL-III, TNC, and MKX using the same protocol described above. RT–qPCR was carried out on cells cocultured with Fe-Ms to investigate the effects of Fe-Ms on osteogenesis and tenogenesis. The primer sequences are listed in Supplementary Table 3.

In vitro evaluation of the immunomodulatory effect

The in vitro immunomodulatory effect of the microrobots was evaluated in an LPS-stimulated macrophage model. The RAW 264.7 macrophage line, provided by the Shanghai Institute of Cells, Chinese Academy of Sciences, was used in this study. RAW264.7 cells were seeded into the lower Transwell chambers (0.4 μm pores) of a 24-well plate overnight. Then, 100 μg/ml LPS was added to the lower chambers, and the microspheres were added to the upper chambers. After incubation for 24 h, the cells were harvested and evaluated. DCFH-DA was used to detect intracellular ROS accumulation by incubating the cells for 30 min. After PBS washed, the macrophages were observed and recorded under an inverted fluorescence microscopy. Cell immunofluorescence staining (carried out for iNOS, CD86, and CD206) and RT–qPCR (carried out for TNF–α, CD86, and CD206) were performed as described above.

In vivo rat RCT model

The animal experiments were approved by the Animal Ethics Committee of West China Hospital, Sichuan University (Approval No.20221114004). A total of 40 SD rats (male, 8-week-old) were randomly divided into 5 groups: the control group, Mg-Ms group, Zn-Ms group, Mg/Zn-Mixed-Ms group and Mg/Zn-Janus-Mr group. All rats were used to establish the RCT model on both forelimbs. Briefly, the rats were anesthetized by inhalation of isoflurane and fixed in the supine position. After shaving, disinfecting, and incising the skin, the deltoid muscle was split and incised to expose the supraspinatus tendon. The supraspinatus tendon was completely severed from the footprint at the greater tuberosity, and the bone surface of the footprint was ground with a drill. Then, a 0.8-mm drill was used to make a bone tunnel in the head of the humerus, and the supraspinatus tendon was reduced back to the greater tuberosity through the bone tunnel using a 5-0 absorbable suture. Before the knot was tied tightly, the microrobots were injected and implanted between the tendon and bone, and a magnet was placed on the humeral side to control the orientation of the microrobots. The deltoid muscle and skin were then closed. At predefined time points (postoperative weeks 4 and 8), half of the rats were subjected to radiological examination, gait analysis, and histological staining (n = 4), while half were subjected to biomechanical tests (n = 4).

Radiological examination

A 7 T animal MRI system (Bruker BioSpec 70/30USR) was used to evaluate the regeneration of the supraspinatus tendon in vivo. At postoperative weeks 4 and 8, the rats were anesthetized by inhalation of isoflurane and underwent MRI scanning. The sagittal T2WI images were processed by Materialise Mimics Innovation Suite Medical 21.0. After the rats were euthanized with an overdose of isoflurane, the supraspinatus–humerus complex was collected and fixed with 4% paraformaldehyde. Bone formation in the humerus was evaluated by micro-CT scanning (Quantum GX micro-CT imaging system).

Gait analysis

Gait analysis was performed to assess the forelimb functional recovery of the rats. A 100 cm × 20 cm blank paper with a dark box at the end was prepared. The rats were placed on the beginning of the paper and allowed to walk freely to the dark box. The footprints of the rats' forepaws were recorded by dying with black ink. Stride length (referring to the distance from one footprint to the next footprint of the same paw) and step length (referring to the distance from the footprint of one paw to the footprint of the other paw) were recorded.

Biomechanical tests

After the rats were euthanized, fresh supraspinatus–humerus complexes were harvested, frozen at −80 °C and thawed before testing. The biomechanical tests of all the samples were performed using a universal mechanical testing machine (3345, INSTRON). The proximal humerus was directly clamped in the testing machine, and the supraspinatus muscle was wrapped with sandpaper to avoid slippage during testing. After a preload of 1 N was applied, each sample was pulled until failure at a constant rate of 5 mm/min. The ultimate load at failure and stiffness of the supraspinatus–humerus complex were recorded.

Histological staining

After the supraspinatus–humerus complex was completely fixed, 10% ethylenediaminetetraacetic acid solution was used to decalcify the samples for 4 weeks. The samples were then dehydrated and embedded in paraffin. Continuously sliced histological sections with a thickness of 5 μm were subjected to HE, Masson, and Sirius Red staining according to the manufacturer's protocol to demonstrate the general histological structure of the samples. A modified histological scoring system was used to quantitatively evaluate regeneration of the TBI (Supplementary Table 4)[75,76].

Multiplex immunofluorescence staining for osteogenic markers (BMP-2 and OCN) and tenogenic markers (COL-I, COL-III, and TNC) was performed on tissues harvested at postoperative weeks 4 and 8.

Macrophage surface markers (CD206 and CD86) was stained on tissues harvested at postoperative week 4. Multiplex immunofluorescence staining was performed separately on continuous slices using the tyramide signal amplification (TSA) kit. Briefly, after antigen retrieval, the slices were blocked and incubated with 100 μl of anti-COL-I or anti-CD206 working solution for 40 min at 37 °C. The slices were then incubated with Opal Polymer HRP secondary antibody for 10 min at 37 °C. After washed with PBS twice, Opal 520 was added for coloration for 10 min at room temperature. Through another round of antigen retrieval and blocking, the slices were incubated with 100 μl of anti-BMP-2 or anti-COL-III working solution followed by Opal Polymer HRP secondary antibody and Opal 570 coloration sequentially. The slices were additionally incubated with 100 μl of anti-OCN, anti-TNC or anti-CD86 working solution followed by Opal Polymer HRP secondary antibody and Opal 650 coloration. After DAPI staining and antifade solution sealing, the slices were scanned using Olympus VS200 system, and the images were analyzed using OlyVIA 3.4.1 software.

Statistical analysis

All the data are presented as the means ± SDs. Statistical analysis was performed via GraphPad Prism (version 9.5.0; GraphPad Software, Inc., CA, USA). Two-sided analysis of variance (ANOVA) was used to determine statistical significance among multiple groups.

Reporting summary

Further information on research design is available in the Nature Portfolio Reporting Summary linked to this article.

Data availability

All the data supporting the findings of this study are available within the article, supplementary information files, and source data file. Source data is available for Figs. 2B–D, 3F, G, 4B, 4E, F, 4H, 5B, 5H, 6D, E, 6G, H, 7B, C, 7E, F, 8B–E, 8G, J, 9B, and 9D–G and Supplementary Figs. 1-2, 10-11, 14, 16-31, and 40-42 in the associated source data file. Source data are provided with this paper.

References

1. Yamamoto, A. et al. Prevalence and risk factors of a rotator cuff tear in the general population. *J. Shoulder Elb. Surg.* **19**, 116–120 (2010).
2. Tashjian, R. Z. Epidemiology, natural history, and indications for treatment of rotator cuff tears. *Clin. Sports Med.* **31**, 589–604 (2012).
3. Amini, M. H., Ricchetti, E. T., Iannotti, J. P. & Derwin, K. A. Rotator cuff repair: challenges and solutions. *Orthopedic Res. Rev.* **7**, 57–69 (2015).
4. Huegel, J., Williams, A. A. & Soslowsky, L. J. Rotator cuff biology and biomechanics: a review of normal and pathological conditions. *Curr. Rheumatol. Rep.* **17**, 476 (2015).
5. Rossetti, L. et al. The microstructure and micromechanics of the tendon-bone insertion. *Nat. Mater.* **16**, 664 (2017).
6. Zhu, C., Qiu, J., Thomopoulos, S. & Xia, Y. Augmenting tendon-to-bone repair with functionally graded scaffolds. *Adv. Healthc. Mater.* **10**, e2002269 (2021).
7. Genin, G. M. et al. Functional grading of mineral and collagen in the attachment of tendon to bone. *Biophys. J.* **97**, 976–985 (2009).
8. Wopenka, B., Kent, A., Pasteris, J. D., Yoon, Y. & Thomopoulos, S. The tendon-to-bone transition of the rotator cuff: a preliminary Raman spectroscopic study documenting the gradual mineralization across the insertion in rat tissue samples. *Appl. Spectrosc.* **62**, 1285–1294 (2008).
9. Chretien A, Couchot M, Mabilleau G, Behets C. Biomechanical, microstructural and material properties of tendon and bone in the young Oim mice model of osteogenesis imperfecta. *Int. J. Mol. Sci.* **23**, 9928 (2022).
10. Thomopoulos, S., Marquez, J. P., Weinberger, B., Birman, V. & Genin, G. M. Collagen fiber orientation at the tendon to bone insertion and its influence on stress concentrations. *J. Biomech.* **39**, 1842–1851 (2006).
11. Zhu, C., Pongkitwitoon, S., Qiu, J., Thomopoulos, S. & Xia, Y. Design and fabrication of a hierarchically structured scaffold for tendon-to-bone repair. *Adv. Mater.* **30**, e1707306 (2018).
12. Qin, B. et al. Engineered exosomes: a promising strategy for tendon-bone healing. *J. Adv. Res.* **64**, 155-169 (2023).
13. Jaworowski, Z., Barbalat, F., Blain, C. & Peyre, E. Heavy metals in human and animal bones from ancient and contemporary France. *Sci. Total Environ.* **43**, 103–126 (1985).
14. Spadaro, J. A., Becker, R. O. & Bachman, C. H. The distribution of trace metal ions in bone and tendon. *Calcif. Tissue Res.* **6**, 49–54 (1970).
15. de Baaij, J. H., Hoenderop, J. G. & Bindels, R. J. Magnesium in man: implications for health and disease. *Physiol. Rev.* **95**, 1–46 (2015).
16. Yuan, Z. et al. Injectable PLGA microspheres with tunable magnesium ion release for promoting bone regeneration. *Acta Biomater.* **85**, 294–309 (2019).
17. Zhao, Z. et al. Capturing magnesium ions via microfluidic hydrogel microspheres for promoting cancellous bone regeneration. *ACS Nano* **15**, 13041–13054 (2021).
18. Rude, R. K., Oldham, S. B., Sharp, C. F. Jr. & Singer, F. R. Parathyroid hormone secretion in magnesium deficiency. *J. Clin. Endocrinol. Metab.* **47**, 800–806 (1978).
19. Chasapis, C. T., Ntoupa, P. A., Spiliopoulou, C. A. & Stefanidou, M. E. Recent aspects of the effects of zinc on human health. *Arch. Toxicol.* **94**, 1443–1460 (2020).
20. Rong, X. et al. An extracellular vesicle-cloaked multifaceted biocatalyst for ultrasound-augmented tendon matrix reconstruction and immune microenvironment regulation. *ACS Nano* **17**, 16501–16516 (2023).
21. Yang, R. et al. Gradient bimetallic ion-based hydrogels for tissue microstructure reconstruction of tendon-to-bone insertion. *Sci. Adv.* **7**, eabg3816 (2021).
22. Calejo, I., Costa-Almeida, R., Reis, R.L. & Gomes, M.E. A textile platform using continuous aligned and textured composite microfibers to engineer tendon-to-bone interface gradient scaffolds. *Adv. Healthc. Mater.* **8**, e1900200 (2019).
23. Dang, G.P. et al. Regulation and reconstruction of cell phenotype gradients along the tendon-bone interface. *Adv. Funct. Mater.* **33**, 2210275 (2023).
24. Luo, Z. et al. Vertical extrusion cryo(bio)printing for anisotropic tissue manufacturing. *Adv. Mater.* **34**, e2108931 (2022).
25. Bai, L. et al. Bioprinted living tissue constructs with layer-specific, growth factor-loaded microspheres for improved enthesis healing of a rotator cuff. *Acta Biomater.* **154**, 275–289 (2022).
26. Du, L. et al. Multicellular bioprinting of biomimetic inks for tendon-to-bone regeneration. *Adv. Sci.* **10**, e2301309 (2023).
27. Chae, S. et al. 3D cell-printing of gradient multi-tissue interfaces for rotator cuff regeneration. *Bioact. Mater.* **19**, 611–625 (2023).
28. Nelson, B. J. & Pané, S. Delivering drugs with microrobots. *Sci. (N. Y., NY)* **382**, 1120–1122 (2023).
29. Kim, Y. & Zhao, X. H. Magnetic Soft Materials and Robots. *Chem. Rev.* **122**, 5317–5364 (2022).
30. Yang, L., Yang, W., Xu, W., Zhao, Y.J. & Shang, L.R. Bio-inspired Janus microcarriers with sequential actives release for bone regeneration. *Chem. Eng. J.* **476**, 146797 (2023).
31. Chen, H. et al. Magnetic hydrogel microrobots delivery system for deafness prevention. *Adv. Funct. Mater.* **33**, 2303011 (2023).
32. Mueen, R. et al. ZnO/CeO2 nanocomposite with low photocatalytic activity as efficient UV filters. *J. Mater. Sci.* **55**, 6834–6847 (2020).

33. Zhang, L. et al. Synthesis of ZnO doped high valence S element and study of photogenerated charges properties. *RSC Adv.* **9**, 4422–4427 (2019).
34. Li, Y., Yang, S., Lu, X., Duan, W. & Moriga, T. Synthesis and evaluation of the SERS effect of Fe3O4–Ag Janus composite materials for separable, highly sensitive substrates. *RSC Adv.* **9**, 2877–2884 (2019).
35. Pardo, A. et al. Magnetically-assisted 3D bioprinting of anisotropic tissue-mimetic constructs. *Adv. Funct. Mater.* **32**, 2208940 (2022).
36. Teixeira, S. P. B. et al. Guiding stem cell tenogenesis by modulation of growth factor signaling and cell-scale biophysical cues in bioengineered constructs. *Adv. Funct. Mater.* **34**, 2312961 (2024).
37. Tang, G.S. et al. Gas-shearing fabrication of multicompartmental microspheres: a one-step and oil-free approach. *Adv. Sci.* **6**, 1802342 (2019).
38. Daly, A. C., Riley, L., Segura, T. & Burdick, J. A. Hydrogel microparticles for biomedical applications. *Nat. Rev. Mater.* **5**, 20–43 (2020).
39. Ravanbakhsh, H. et al. Emerging technologies in multi-material bioprinting. *Adv. Mater.* **33**, e2104730 (2021).
40. Huang, D.Q., Wang, J.L., Nie, M., Chen, G.P. & Zhao, Y.J. Pollen-inspired adhesive multilobe microparticles from microfluidics for intestinal drug delivery. *Adv. Mater.* **35**, 2301192 (2023).
41. Song, T., Zhang, H., Luo, Z., Shang, L. & Zhao, Y. Primary human pancreatic cancer cells cultivation in microfluidic hydrogel microcapsules for drug evaluation. *Adv. Sci.* **10**, e2206004 (2023).
42. Tang, G.S. et al. Designable dual-power micromotors fabricated from a biocompatible gas-shearing strategy. *Chem. Eng. J.* **407**, 127187 (2021).
43. Ding, Z. et al. Janus-structured microgel barrier with tissue adhesive and hemostatic characteristics for efficient prevention of post-operative adhesion. *Small* **20**, e2403753 (2024).
44. Chaudhuri, O. et al. Hydrogels with tunable stress relaxation regulate stem cell fate and activity. *Nat. Mater.* **15**, 326–334 (2016).
45. Lee, K. Y. & Mooney, D. J. Alginate: properties and biomedical applications. *Prog. Polym. Sci.* **37**, 106–126 (2012).
46. Wang, L., Kim, Y., Guo, C. F. & Zhao, X. Hard-magnetic elastica. *J. Mech. Phys. Solids* **142**, 104045 (2020).
47. Yi, S. et al. High-throughput fabrication of soft magneto-origami machines. *Nat. Commun.* **13**, 4177 (2022).
48. Bonnevie, E. D. & Mauck, R. L. Physiology and engineering of the graded interfaces of musculoskeletal junctions. *Annu. Rev. Biomed. Eng.* **20**, 403–429 (2018).
49. Maffulli, N., Barrass, V. & Ewen, S. W. Light microscopic histology of Achilles tendon ruptures. A comparison with unruptured tendons. *Am. J. Sports Med.* **28**, 857–863 (2000).
50. Millar, N. L. et al. MicroRNA29a regulates IL-33-mediated tissue remodelling in tendon disease. *Nat. Commun.* **6**, 6774 (2015).
51. Cho, Y. et al. CTRP3 exacerbates tendinopathy by dysregulating tendon stem cell differentiation and altering extracellular matrix composition. *Sci. Adv.* **7**, eabg6069 (2021).
52. Xu, K. et al. Tenascin-C regulates migration of SOX10 tendon stem cells via integrin-α9 for promoting patellar tendon remodeling. *BioFactors* **47**, 768–777 (2021).
53. Kayama, T. et al. Gtf2ird1-Dependent Mohawk Expression Regulates Mechanosensing Properties of the Tendon. *Mol. Cell. Biol.* **36**, 1297–1309 (2016).
54. Yuan, Z. et al. Controlled magnesium ion delivery system for in situ bone tissue engineering. *J. Controll. Release. Off. J. Controll. Release. Soc.* **350**, 360–376 (2022).
55. Ding, Z. C., Lin, Y. K., Gan, Y. K. & Tang, T. T. Molecular pathogenesis of fracture nonunion. *J. Orthop. Transl.* **14**, 45–56 (2018).
56. Luo, Z.Y. et al. 3D Assembly of cryo(bio)printed modular units for shelf-ready scalable tissue fabrication. *Adv. Funct. Mater.* **34**, 2309173 (2023).
57. Gonzalez-Fernandez, T., Tenorio, A. J., Campbell, K. T., Silva, E. A. & Leach, J. K. Alginate-based bioinks for 3D bioprinting and fabrication of anatomically accurate bone grafts. *Tissue Eng. Part A* **27**, 1168–1181 (2021).
58. Chen, M. et al. Biceps detachment preserves joint function in a chronic massive rotator cuff tear rat model. *Am. J. Sports Med.* **46**, 3486–3494 (2018).
59. Feichtinger, X. et al. Substantial biomechanical improvement by extracorporeal shockwave therapy after surgical repair of rodent chronic rotator cuff tears. *Am. J. Sports Med.* **47**, 2158–2166 (2019).
60. Wang, T. et al. Engineering immunomodulatory and osteoinductive implant surfaces via mussel adhesion-mediated ion coordination and molecular clicking. *Nat. Commun.* **13**, 160 (2022).
61. Cheng, P. et al. High-purity magnesium interference screws promote fibrocartilaginous entheses regeneration in the anterior cruciate ligament reconstruction rabbit model via accumulation of BMP-2 and VEGF. *Biomaterials* **81**, 14–26 (2016).
62. Chen, B.J. et al. Sustained release of magnesium ions mediated by injectable self-healing adhesive hydrogel promotes fibrocartilaginous interface regeneration in the rabbit rotator cuff tear model. *Chem. Eng. J.* **396**, 125335(2020).
63. Han, X. et al. Lotus seedpod-inspired internal vascularized 3D printed scaffold for bone tissue repair. *Bioact. Mater.* **6**, 1639–1652 (2021).
64. Liu, A. et al. Nitric oxide nanomotor driving exosomes-loaded microneedles for Achilles tendinopathy healing. *ACS Nano* **15**, 13339–13350 (2021).
65. Wang, Y. et al. Functional regeneration and repair of tendons using biomimetic scaffolds loaded with recombinant periostin. *Nat. Commun.* **12**, 1293 (2021).
66. Du, L., Wu, J., Han, Y. & Wu, C. Immunomodulatory multicellular scaffolds for tendon-to-bone regeneration. *Sci. Adv.* **10**, eadk6610 (2024).
67. Gao, H. et al. Regulating macrophages through immunomodulatory biomaterials is a promising strategy for promoting tendon-bone healing. *J. Funct. Biomater.* **13**, 243 (2022).
68. Gao, H. et al. Bi-lineage inducible and immunoregulatory electrospun fibers scaffolds for synchronous regeneration of tendon-to-bone interface. *Mater. Today Bio* **22**, 100749 (2023).
69. Zou, J. et al. Therapeutic potential and mechanisms of mesenchymal stem cell-derived exosomes as bioactive materials in tendon-bone healing. *J. Nanobiotechnology* **21**, 14 (2023).
70. Kawamura, S., Ying, L., Kim, H. J., Dynybil, C. & Rodeo, S. A. Macrophages accumulate in the early phase of tendon-bone healing. *J. Orthop. Res.: Off. Publ. Orthop. Res. Soc.* **23**, 1425–1432 (2005).
71. Li, J. et al. Controlled-release hydrogel loaded with magnesium-based nanoflowers synergize immunomodulation and cartilage regeneration in tendon-bone healing. *Bioact. Mater.* **36**, 62–82 (2024).
72. Chen, Z. et al. Mesenchymal stem cells and macrophages and their interactions in tendon-bone healing. *J. Orthop. Transl.* **39**, 63–73 (2023).
73. Zhang, X. et al. Engineered metallic ion-based hydrogel for tendon-bone reconstruction. *ACS Appl. Mater. Interfaces* **16**, 6837–6848 (2024).
74. Li, R. et al. Graded modulation of inflammation by metal ion-coordinated peptide-based hydrogel chemical regulators promotes tendon-bone junction regeneration. *ACS Appl. Mater. Interfaces* **16**, 46145–46158 (2024).
75. Chen, C. et al. Engineering an enthesis-like graft for rotator cuff repair: An approach to fabricate highly biomimetic scaffold capable

of zone-specifically releasing stem cell differentiation inducers. *Bioact. Mater.* **16**, 451–471 (2022).
76. Han, F. et al. Nano-calcium silicate mineralized fish scale scaffolds for enhancing tendon-bone healing. *Bioact. Mater.* **20**, 29–40 (2023).

Acknowledgements

This work was supported by the National Natural Science Foundation of China (82302786 Z. L.; 82172394, U22A20280 and 81873987 Z. Z.), National Key Research and Development Program of China (2022YFC2503100 and 2022YFC2503104 Z. Z.), The China Postdoctoral Science Foundation (BX20230245 and 2023M742478 Z. L.), Sichuan Science and Technology Program (2023YFH0068 Z. L.), the Sichuan Province Innovative Talent Funding Proiect for Postdoctoral Fellows (BX202203 Z. L.), 1.3.5 project for disciplines of excellence, West China Hospital, Sichuan University (ZYGD23033 Z. Z.). We gratefully acknowledge Li Li, Fei Chen, and Chunjuan Bao of the Institute of Clinical Pathology, Sichuan University, for processing histological staining. We also gratefully acknowledge for the technical assistance of Core Facility of West China Hospital (Li Chai, Yi Li, Xing Xu, Yaping Wu, Lei Wu, and Bo Su).

Author contributions

Z. D. designed the research. Z. D., Y. C., H. S., J. F., Y. L., Z. L. (Zhimin Liang), and C. H. performed the experiments. Z. D., Y. C., P. L., and Z. L. (Zeyu Luo) analyzed the data. Z. D., X, R., and X. F. wrote the manuscript. S. Y. and L. W. performed the equation derivation. G. T., Z. Z., and Z. L. (Zeyu Luo) supervised the research. All authors discussed the results and commented on the manuscript.

Competing interests

The authors declare no competing interests.

Additional information

Supplementary information The online version contains supplementary material available at https://doi.org/10.1038/s41467-025-57499-x.

Correspondence and requests for materials should be addressed to Guosheng Tang, Zongke Zhou or Zeyu Luo.

Peer review information *Nature Communications* thanks Cato Laurencin and the other, anonymous, reviewers for their contribution to the peer review of this work. A peer review file is available.